Z. Phys. A 357, 215–234 (1997)

ZEITSCHRIFT
FÜR PHYSIK A
© Springer-Verlag 1997

Charged pion production in Au on Au collisions at 1 AGeV

The $FOPI$ Collaboration

D. Pelte[6], E. Häfele[6], D. Best[4], G. Goebels[6], N. Herrmann[4,6], C. Pinkenburg[4], W. Reisdorf[4], M. Trzaska[6], J.P. Alard[3], V. Amouroux[3], A. Andronic[1], Z. Basrak[11], N. Bastid[3], I. Belyaev[7], J. Biegansky[5], A. Buta[1], R. Čaplar[11], N. Cindro[11], J.P. Coffin[9], P. Crochet[9], P. Dupieux[3], M. Dželalija[11], J. Erö[2], M. Eskef[6], P. Fintz[9], Z. Fodor[2], A. Genoux-Lubain[3], A. Gobbi[4], G. Guillaume[9], K.D. Hildenbrand[4], B. Hong[4], F. Jundt[9], J. Kecskemeti[2], M. Kirejczyk[4,10], P. Koncz[2], M. Korolija[11], Y. Korchagin[7], R. Kotte[5], C. Kuhn[9], D. Lambrecht[3], A. Lebedev[7], I. Legrand[1], Y. Leifels[4], V. Manko[8], H. Merlitz[4,6], J. Mösner[5], S. Mohren[6], D. Moisa[1], W. Neubert[5], M. Petrovici[1], P. Pras[3], F. Rami[9], V. Ramillien[3], J.L. Ritman[4], C. Roy[9], D. Schüll[4], Z. Seres[2], B. Sikora[10], V. Simion[1], K. Siwek-Wilczynska[10], V. Smolyankin[7], U. Sodan[4], M.A. Vasiliev[8], P. Wagner[9], G.S. Wang[4], T. Wienold[4], D. Wohlfarth[5], A. Zhilin[7]

[1] Institute for Physics and Nuclear Engineering, Bucharest, Romania
[2] Central Research Institute for Physics, Budapest, Hungary
[3] Laboratoire de Physique Corpusculaire, IN2P3/CNRS, and Université Blaise Pascal, Clermont-Ferrand, France
[4] Gesellschaft für Schwerionenforschung, Darmstadt, Germany
[5] Forschungszentrum Rossendorf, Dresden, Germany
[6] Physikalisches Institut der Universität Heidelberg, Heidelberg, Germany
[7] Institute for Theoretical and Experimental Physics, Moscow, Russia
[8] Kurchatov Institute, Moscow, Russia
[9] Centre de Recherches Nucléaires and Université Louis Pasteur, Strasbourg, France
[10] Institute of Experimental Physics, University of Warsaw, Poland
[11] Rudjer Boskovic Institute, Zagreb, Croatia

Received: 15 July 1996 / Revised version: 23 October 1996
Communicated by V. Metag

Abstract. Charged pions are measured with the 4π detector $FOPI$ at GSI using the Au on Au reaction at 1.06 AGeV bombarding energy. The pion multiplicities n_π increase with the number of participants $A_{\rm part}$. The average pion multiplicities per participant are $\frac{<n_{\pi^-}>}{<A_{\rm part}>} = 0.0308$ and $\frac{<n_{\pi^+}>}{<A_{\rm part}>} = 0.0182$. These values are only half as large as extrapolated from the low-mass systems studied by Harris et al. The ratio $\frac{n_{\pi^-}}{n_{\pi^+}}$ increases with $A_{\rm part}$ and decreases with the pion kinetic energies. The pion kinetic energy spectra have concave shapes, their parametrization in terms of thermal Boltzmann distributions yields a low ($T_{{\rm l},\pi}$) and high ($T_{{\rm h},\pi}$) temperature which change with the cm emission angle Θ of the pions. In the angular range $45° < \Theta < 135°$ the low temperature $< T_{{\rm l},\pi^-} >$ is larger than $< T_{{\rm l},\pi^+} >$, the high temperatures $< T_{{\rm h},\pi^-} >$, $< T_{{\rm h},\pi^+} >$ are, within experimental uncertainties, the same. The inclusive polar angular distributions of pions are anisotropic, $d\sigma/d\Omega$ increases for forward and backward angles. The forward - backward enhancements are independent of the pion kinetic energies or the number of participants. In addition to the preferred forward - backward emission, also the enhanced emission into the transverse direction $\Theta = 90°$ is observed for pions with high energies or for pions from near-central collisions. These observations and the shape of the rapidity spectra suggest that pions, emitted from the central rapidity region, are partly rescattered by spectator matter. The strength of the rescattering process depends only weakly on the number of participants. The experimental data are compared to the results of $IQMD/GEANT$ calculations using momentum dependent NN interactions and a hard equation of state. The calculated pion multiplicities are approximately 50% larger than experimentally determined; the existence of secondary pion sources is reproduced by the calculation, but their predicted strengths are larger than experimentally observed.

PACS: 25.75.+r; 14.40.Aq

1 Introduction

For more than two decades now the investigation of nucleus - nucleus collisions at relativistic and ultra relativistic energies has attracted the interest of physicists. Such collisions are the only way to transform nuclear matter from its ground state into states of high density and temperature and reach, albeit for only a very short moment, the situation which prevailed at the early times of the universe. Already at the lower energy limit of 1 AGeV the baryon density is predicted to reach peak densities of 3 times normal nuclear matter density, the peak temperatures are of the order of 100 MeV [1–3]. Under such conditions new particles are produced, most abundantly charged and neutral pions.

Until 1980 the experiments in the energy range around 1 AGeV were concentrated at the *BEVALAC* laboratory. After pioneering experiments to measure the inclusive cross

sections of charged pions [4], the possibility to obtain π exclusive data was opened by the *streamer chamber group* [5] and the *plastic ball group* [6]. The accumulated results of these and other groups were reviewed in a paper by Stock [7]. The most important conclusion was that the measured pion production cross sections are smaller than theoretically predicted at that time. This led to the hypothesis that a large portion of the kinetic energy is converted into compression energy which suggests the existence of a hard equation of state for nuclear matter. Since then theoretically more advanced techniques were developed to treat the processes of particle production, c.f. [1–3, 8–17] for a representative list of recent theoretical publications. It was realized that pion production is a multi-step process which extends to the late stages of the collision. The recent discovery of a strong radial flow using nucleon clusters as sensitive probes [18–20] implies that cooling during the expansion phase is an important mechanism which could limit the pion multiplicities to the values observed at freezeout [17, 21]. On a more speculative level the existence of density isomers was proposed as a factor possibly influencing pion production [22].

Despite many earlier studies the pion momentum space distribution, under reasonably exclusive conditions, is still incompletely known. It seems evident that the full, i.e. 4π momentum space distribution of the pions of all three charges could serve as a valuable constraint to theoretical models, and would allow to determine the integrated pion multiplicities without the need to extrapolate into unmeasured regions of phase space.

The experimental investigation of pion production requires an apparatus which not only identifies the charge number Z but also the mass number A of all produced particles, preferably in the total 4π solid angle. For charged pions this task can be accomplished by a magnetic spectrometer, for neutral pions a large gamma ray spectrometer is required to identify the $\pi^0 \rightarrow \gamma + \gamma$ decay channel. Recently, at the SIS facility of GSI a two-arm photon spectrometer, $TAPS$ [23], and two magnetic spectrometers to study meson production, $KaoS$ [24] and $FOPI$ [25], were constructed. First results from the $KaoS$ spectrometer for charged mesons [26–30] and from the $TAPS$ spectrometer for neutral mesons [31–34] have become available. The $FOPI$ spectrometer is a 4π detector which had its precursor in the $DIOGENE$ detector at *SATURNE/Saclay* [35]. As a 4π detector $FOPI$ detects all charged reaction products in almost complete phase space. With the $FOPI$ spectrometer both π^- and π^+ are simultaneously measured and possible differences can be recognized under identical experimental conditions.

The present paper is the first in a series of papers which study the pion production in nucleus - nucleus collisions at SIS energies. We will start in the following section by describing the FOPI detector and then discuss in details our tracking methods. In Sect. 3 we will present our results on charged pion multiplicities, and give a detailed account of their momentum distributions together with phenomenological parameterizations. Section 4 presents a comparison with Quantum Molecular Dynamics [10–12] calculations. In subsequent papers we will compare the phenomena observed in the Au + Au system with those of lighter mass systems. We will extend the analysis to study the flow patterns in the pion phase space distributions, and we will attempt to identify the excited Baryon resonances which serve, via their decay, as main contributors to the experimental pion yields.

2 Experimental procedures

The reaction Au + Au was studied at a nominal energy of 1.06 AGeV. The Au beam was accelerated by the $UNILAC/SIS$ accelerator combination of the GSI/Darmstadt. The duty cycle was 75% with a spill length of 4 s. The average beam intensity corresponded to $3 \cdot 10^5$ particles per spill. The target consisted of an Au foil of 100 μm thickness. This corresponds to an interaction probability of 0.5%. The average energy loss of the Au beam in this foil amounts to 0.006 AGeV and was neglected.

Before hitting the target the beam had to pass through a 100 μm thin scintillator foil which was mounted 2.5 m upstream from the target inside the vacuum of the beam transport system. The signals from this foil served as input into the beam counter, and they provided also the time reference for the data acquisition system and for all time-of-flight measurements. The target itself was positioned outside the vacuum to avoid the energy loss of particles in the walls of the vacuum vessel. The target was mounted inside a pipe of aluminized mylar foil which ran through the complete $FOPI$ detector and which was filled with *He*. The purpose of using *He* was to minimize the beam interactions with non-target material. A 125 μm thin Kapton foil separated the vacuum system from the mylar pipe. The beam was positioned on the target by two active collimators, one close to the beam counter, the other 30 cm upstream from the target. The beam spot size was of the order of a few mm. The number of registered events was close to 10^6, for the analysis presented here a subsample of approximately 10^5 events was used. This limitation is caused by the extended time necessary to calibrate and analyze the data from the various detector components. The complete data sample is used in the not yet completed study of $\pi\pi$ and πp correlations.

In the following sections a number of conventions shall be used: All quantities which refer to the laboratory or target system will be labelled by small letters, small letters with a prime will be used for quantities which refer to the projectile system. The center of mass or fireball system is generally characterized by capital letters. Exceptions are those quantities, like the transverse momentum, which remain unchanged under system transformations. The magnitude of the transverse momentum p_t is given in units of $p_t^{(0)}$ where the index (0) indicates, in agreement with previous $FOPI$ publications [36–41], a normalization by the factor $(A \cdot P_{\rm proj}/A_{\rm proj})^{-1}$ and where A is the particle's mass number. Similarly the rapidity Y in the cm system is normalized by the factor $(Y_{\rm proj})^{-1}$ and this quantity is labelled $Y^{(0)}$. Under the present conditions the normalization factor for the pion transverse momentum has the value $9.47({\rm GeV/c})^{-1}$ and for the rapidity one obtains a normalization factor 1.44. Finally the letter E stands for the total energy in the center of mass system, the rest mass m of a particle is given in units of MeV so that the kinetic energy in the cm system is $E - m$.

2.1 The $FOPI$ detector

The $FOPI$ detector is a modular detection system with almost 4π coverage which was put into operation in two steps, called phase 1 and phase 2. The phase 1 includes the forward detectors, their properties were described in detail in [25]. The outer plastic wall PLA which is part of the phase 1 components served as main trigger in the present experiment. It starts the data readout whenever the measured particle multiplicity in the PLA is within a specified range. Three such ranges were defined, i.e. range 1: $8 < n_{\rm PLA} < 100$, range 2: $30 < n_{\rm PLA} < 100$, range 3: $70 < n_{\rm PLA} < 100$. The relative contribution of these multiplicity ranges to the accepted data was controlled by scale-down factors which were set to $128 : 4 : 1$.

At the time of the experiment the phase 2 was not yet completed, it consisted of the superconducting solenoid which houses the central drift chamber (CDC) with the target in its centre at $x, y, z = 0, 0, 0$. The CDC is a pictorial wire chamber of the jet type, with the wires parallel to the beam direction. Its outer length is 200 cm, its inner diameter is 40 cm and its outer diameter 160 cm. The chamber has 16 sectors which are tilted against the radial direction by 8°. Each sector has an anode plane with 60 sense wires. The staggering distance between adjacent sense wires is ± 200 μm. The main difference of the CDC to other drift chambers, e.g. the $OPAL$ drift chamber [42], is its forward wall. The forward wall has the shape of a cone with 30° opening, the wall is made of epoxy with a thickness of 4 mm. Similarly the materials of the inner (STYRODUR) and outer (honey-comb type epoxy) cylinders were kept at minimum thickness. A more detailed description of the components of the phase 2 will be published once the $FOPI$ detector is completed.

The CDC is operated at a nominal pressure of 1 bar with a gas mixture of 88% Ar, 10% iC_4H_{10} and 2% CH_4. Under normal conditions the gas volume of the CDC is exchanged every 50 h. The electric drift field has a value of 710 V/cm, the electron drift velocity is then v_d = 43.7 μm/ns. The magnetic field produced by the superconducting solenoid has a value of 0.6 T, its inhomogenity over the CDC volume amounts to less than 1%. This field strength causes a Lorentz angle of $\alpha_{\rm L}$ = 32°, by which the electron drift direction deviates from the vertical direction onto the sense wire plane.

The electron pulses on the sense wires are read out at both ends in the common stop mode by a STRUCK DL 363 FADC system. The system runs with a frequency of 100 MHz on a cyclic memory of 1024 addresses, the depth per address is 8 bit nonlinear. Altogether the system has 1920 channels, but only 1808 channels are used for the CDC data, the rest is available for additional control information. The data transfer from the FADC system into the front-end data acquisition system is close to 5 MBytes per second. Besides the control of the FADC system the main purpose of the front-end system is the fast data reduction and organization for the subsequent transfer to the main data storage system. The reduction algorithm runs on a bank of 36 parallel Motorola 68040 CPU's which were purchased from ELTEC (E7). The data reduction yields for each end of a sense wire the electron arrival time t and the accumulated charge q. The time is later used to determine the point of gas ionization

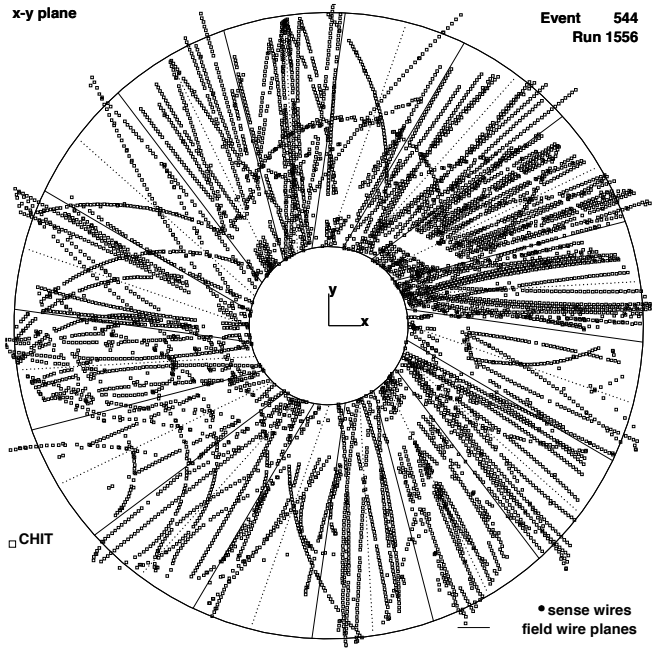

Fig. 1. Hit distribution of tracks from a central event in the x, y plane of the CDC

in the plane perpendicular to the beam axis (x, y plane), the charge is used to determine the position of this point along the sense wire (z direction) and to determine the size de of the ionization. This raw information shall be called a 'hit'. The reduction algorithm has special features which allow the recognition of overlapping electron pulses, i.e. close hits, and the appropriate de correction.

The main data storage system collects all data from the various components of the $FOPI$ detector and dumps them onto tape. It also allows to supervise these components. For example Fig. 1 displays the CDC hit picture in the x, y plane as it is generated by the supervising program. The number of tracks in this picture is approximately 160 which corresponds to 80 particles because of the left-right ambiguity. This ambiguity arises since, without tracking, one cannot decide whether the hit was on the left or right side of the sense wire plane. The assignment of hits to a track has to be performed by special algorithms which are described in the next subsection. During the tracking procedure the left-right ambiguity is resolved by either using the staggering of the sense wires or the sector tilt which allows only one of the two track candidates to pass through the target. But even without tracking Fig. 1 allows certain characteristic features to be distinguished. Most of the tracks have positive and small curvature, they are mainly due to protons. The tracks with negative curvature are readily identified, they correspond to π^-. Tracks with large curvature may curl inside the CDC, sometimes after having experienced a considerable energy loss in the material surrounding the gas volume. It is apparent that there exists a large probability that tracks will cross each other, and that the average number of hits per track is smaller than 60 (c.f. Subsect. 2.3). With the large number of hits (around 5000 in Fig. 1) it is also conceivable that the probability to find hits which by chance form a circle is not negligible. Such tracks shall be called spurious. The number

of spurious tracks is related to the precision with which the CDC has been calibrated, i.e. the measured quantities time t and charge q were converted to x, y, z, de. In the present analysis the calibration was performed in several steps. The first and very raw calibration uses the pulser which allows to compensate time and gain shifts on the individual wires. From then on a self-calibration method is used for the CDC. This method requires an initial set of the parameters drift velocity v_d, Lorentz angle $\alpha_{\rm L}$ and total time shift t_0 which allow a tracking algorithm to identify tracks. These tracks are then used to minimize the hit deviation from the track by varying $v_d, \alpha_{\rm L}, t_0$. Finally, specially selected tracks are used to fine-tune the individual wire corrections.

2.2 Tracking methods

In order to analyze the data from the CDC different tracking algorithms were developed which use different methods to assign the measured hits to the particle tracks. These methods can be principally separated into local and global methods. The local methods are sequential, they assign hits to a track by using the track parameters deduced from previous assignments. After a new assignment the track parameters are recalculated. As a special condition the track may be forced to originate from a fixed vertex position. But this condition is not a requirement for the local methods to work. Therefore local methods may be used to identify secondary vertices. On the other hand global methods perform a hit transformation which allows all possible hits to be assigned simultaneously to one track. But to perform this transformation the vertex position normally has to be known. Notice that the track fitted to the assigned hits, which are then called track points, not necessarily has to pass through this vertex, because hits are measured with finite accuracy.

In the analysis of the data from the CDC both methods were applied. Since the global method used here and called 'conformal mapping (cm)', is slower than local methods (lc) the first step of the analysis always uses the local method. The purpose of this technique is to identify first the 'easy' tracks, i.e. tracks with a large number of hits and small curvature, and thus to reduce the number of not assigned hits. Then the cm algorithm performs the track search on the remaining hit sample. Depending on whether the cm algorithm does not or does use the vertex position determined by the preceeding lc algorithm we call these tracking methods I or II. The tracking method III uses only the lc algorithm with the vertex position assumed to be close to $x = 0, y = 0$. In the following the performance of the track search is described in larger detail for method I.

The number of points on a track may vary between the minimum allowed number $n_{\rm hit} = 10$ and the maximum number $n_{\rm hit} = 60$. For tracks with large curvature the number of points can exceed the upper limit but these instances are very rare. The $n_{\rm hit}$ distribution is shown in Fig. 2 for all tracks, and more specifically for the identified pion tracks. The average number of points per track is $n_{\rm hit} = 40$, for pion tracks this number is 25% smaller which is due to their minimum ionization and due to their high probability to cross other tracks. Since hits near the crossing of two tracks cannot be unambiguously assigned to one track these hits are

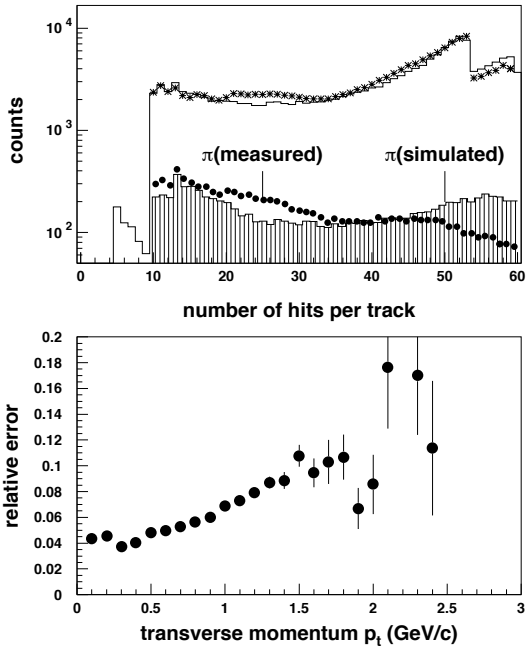

Fig. 2. *Top:* Number distribution of hits per track in the CDC, measured (*stars*) and simulated (*histogram*). The shaded histogram gives the same information for the simulated pions, whereas the black dots correspond to the measured pions. *Bottom:* Relative error $\sigma_{\rm p_t}/p_t$ of the transverse momentum p_t in simulated particle tracks

removed from the hit sample. For pion tracks the standard deviations of the points from the track are in the x, y plane: $\sigma_{\rm x,y} = 1.04$ mm, in the ϑ coordinate: $\sigma_\vartheta = 4.4°$, and the energy loss resolution is: $\sigma_{\rm de}/de = 0.44$. These values are representative for the conditions under which the tracking with the lc and cm algorithms was performed. The values will change when these conditions change. It is obvious that each tracking algorithm has a number of adjustable parameters, like the allowed point deviation from the track in the x, y plane or the size of the $\Delta\vartheta$ range which specifies the upper limit of the allowed point deviation in the ρ, z plane, where $\rho^2 = x^2 + y^2$. Normally a $\Delta\vartheta$ range of 12° was chosen to account for the helix form of the tracks in the ρ, z plane, but in the extreme case one may choose $\Delta\vartheta = 60°$. However in this latter case the particular problem occurs for tracks with transverse momentum $p_t < 100$ MeV/c which curl inside the CDC. These tracks become ambiguous since π^+ cannot be distinguished from π^-. An estimate of how frequently such ambiguities occur may be gained by varying the $\Delta\vartheta$ range.

In the final stage of the track identification the results of all tracking procedures are combined to yield the total track multiplicity. At the same time it is checked whether or not 2 tracks from different tracking algorithms actually belong to the same particle. This might happen since the methods to assign hits to tracks are different for different algorithms. The criteria which recognize double track counting require that the two tracks deviate with respect to the azimuthal angle φ by not more than 5°, and with respect to the transverse momentum p_t by not more than 15%. They also require that more than 90% of the points on each track were measured with different wires. In case double track counting has oc-

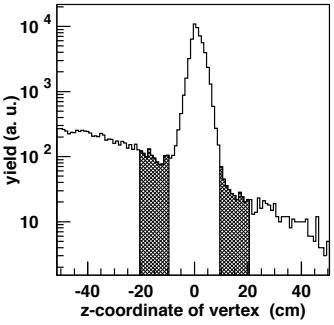

Fig. 3. Distribution of the event vertex z_V along the beam axis. The shaded areas are used to estimate the background contribution within $|z_V| < 10$

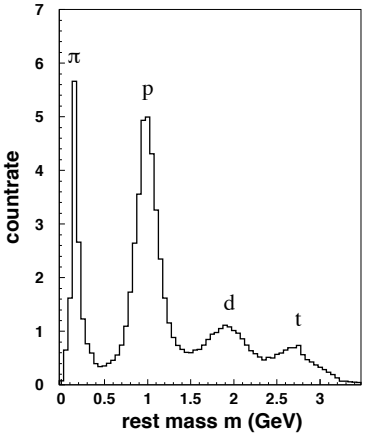

Fig. 4. Mass spectrum of $Z = 1$ particles measured with the CDC

curred these hits are combined and the circle fit is repeated. Finally all tracks are used to calculate the common event vertex in the x, y plane and along the z axis. The track fitting is then repeated by requiring that all tracks pass through the event vertex in the x, y plane and through the mean value of all event vertices on the z axis which should coincide with the $z = 0$ location of the target and which is called reaction vertex.

The location of the reaction vertex was determined, with all tracking parameters set to maximally allowed values, to be $x_V = 0 \pm 0.17$ cm, $y_V = 0 \pm 0.15$ cm, and $z_V = 1.07 \pm 2.48$ cm. A standard deviation $\sigma_z = 3$ cm for z_V is included in the calculation of the error σ_ϑ of the polar angle ϑ. The reduced accuracy to determine the z coordinate of the reaction vertex is due to the inferior method (charge division) in measuring the z coordinate of track points. Nevertheless the z coordinate of the event vertex was used to effectively eliminate background reactions. The procedure can be understood from Fig. 3 which shows the distribution of the event vertex z_V along the z axis. Reactions were only considered as target reactions when $|z_V| < 10$ cm. The shaded areas in Fig. 3 represent those regions of z_V which were used to estimate the background contribution to the accepted events. From the number of events inside these areas one derives a 9% background contribution. Notice that the background contribution depends on the track multiplicity. It becomes strongest in events with very low multiplicity where it increases up to 40%, and is completely negligible for events with large multiplicity. Furthermore if one considers the charged pions alone then the background contribution reduces to a multiplicity averaged value of $3 \pm 1\%$.

Figure 4 displays the mass spectrum of identified particles after the data from the CDC were scanned by the tracking method I. The mass identification is based on the momentum dependence of the particle's energy loss in the CDC gas which closely follows the Bethe-Bloch formula. Notice that π^+ and p can only be separated up to a limit in momentum which was set to $p < 0.65$ GeV/c. Such an identification limit does not exist under the present conditions for the π^-. The peak to background ratio for pions in Fig. 4 is of the order of 15 : 1, the background has, with decreasing importance, its origin in the limited energy loss resolution, spurious tracks, and non-target reactions. It it possible to improve the peak to background ratio by changing the tracking conditions but only with the loss of efficiency which was of the order of 100% for Fig. 4. Pions are selected from Fig. 4 by setting a mass gate $m_\pi < 400$ MeV, which for pion momenta $p > 400$ MeV/c is replaced by a de gate, $\Delta de/de < 0.4$, along the Bethe-Bloch curve for pions.

The problems of accuracy and, more generally, of how efficient tracks are identified can be studied in several ways. Most directly part of the results from the present experiment can be compared to equivalent results from other experiments. The most prominent source for such a comparison is the $KaoS$ experiment at GSI [26–30]. The comparison was made whenever possible, its outcome is shown in Sect. 3. Another way is to analyze the same data from the CDC with the different tracking methods I, II, III. The results quoted here are the means of these three analyses, the differences between them are treated as systematic errors. The systematic error is quoted as second entry into the listed error, the first entry gives the statistical error. If only one error is shown, as for example in the figures, it is usually the larger of the two. Finally the performance of the track finding procedures can be studied by means of Monte Carlo calculations which include a complete simulation of the hit generation in the CDC. For the tracking method I this study is presented in the next subsection.

2.3 Performance test by means of Monte Carlo simulations

The performance of the tracking method I was studied by generating simulated tracks with the $IQMD + GEANT$ event generator. The $IQMD$ model [1, 9–12] was developed with the special purpose to include the dominant mechanisms which lead to pion production. The dominant channel is $N + N \rightarrow N + \Delta$, where the Δ subsequently decays via $\Delta \rightarrow N + \pi$. But also the reverse process occurs which causes pion absorption. Similarly the channel $N + \Delta \rightarrow N + N$ causes Δ absorption before it can decay. The $IQMD$ model includes Coulomb interaction between charged particles and it conserves isospin. In its present version it uses a hard equation of state ($K = 380$ MeV) and momentum dependent NN interactions.

The $GEANT$ program is distributed by $CERN$ [43] and allows to simulate the interaction of particles with matter, where the matter can be a specific detector with all its components. For the present purpose the $GEANT$ program was extended to include the drift of the electrons, produced

Table 1. Relative number of tracked pions which could be matched to the pions from $IQMD$ simulations within the accuracies σ_φ, σ_ϑ and σ_{p_t}/p_t. For unmatched pions the identification within the $IQMD$ sample was impossible. The differences between the tracking modes **a,b,c,d** are explained in the text

	mode			
	a	b	c	d
# of matched π^-	64 %	90 %	91 %	90 %
# of unmatched π^-	8 %	22 %	26 %	24 %
# of unmatched π^- ($p_t > 0.1\,\mathrm{GeV/c}$)	4 %	8 %	11 %	8 %
# of matched π^+	47 %	77 %	88 %	79 %
# of unmatched π^+	5 %	28 %	42 %	38 %
# of unmatched π^+ ($p_t > 0.1\,\mathrm{GeV/c}$)	5 %	17 %	21 %	17 %
σ_φ	0.6^o	0.6^o	0.6^o	0.6^o
σ_ϑ	4.2^o	4.6^o	4.6^o	4.6^o
σ_{p_t}/p_t	0.071	0.073	0.073	0.060

by the ionization of the CDC gas, through this gas towards the anode plane of the CDC and the pulse generation on the wires of this plane. These pulses are then processed by the same program which runs in the front end processors of the data acquisition system, the resulting hit structure is analyzed by the identical tracking algorithms used in the experimental data analysis.

The $IQMD + GEANT$ data sample consists of 10000 events which are weighted with the correct bdb dependence where b is the impact parameter. This condition shall be called henceforth 'minimum bias'. The quality with which the properties of the CDC are simulated by the $GEANT$ program may be judged from the number of accepted hits per track which is compared to the measured distribution for all tracks, and particularly for identified pion tracks, in Fig. 2. This comparison is made in such a way that the total number of tracks is the same in the experiment and the $IQMD + GEANT$ simulation. The number of points per track on measured and simulated tracks differ by only 0.7%. This difference becomes larger when one selects pion tracks. The average number of points on simulated pion tracks is $n_{\mathrm{hit}} = 34$, on the measured tracks the number is 14% smaller. In the experiment and the simulation, the reduction of points is particularly pronounced for positive pion tracks, on the average they have 25% less points than the negative pion tracks. The reduction is probably caused by the crossing of positive pion tracks with other tracks which occurs at small intersection angles. The accuracies of simulated pion tracks are $\sigma_{\mathrm{x,y}} = 0.83$ mm, $\sigma_\vartheta = 2.2^\circ$, and $\sigma_{\mathrm{de}}/de = 0.47$. These values are in close agreement with those obtained from the experimental data in Subsect. 2.2, except for σ_ϑ where the simulation produces a 2 times better resolution. The main reason for this reduction is the improved determination of the z coordinate along the sense wires, which is also noticed in the better accuracy of the vertex localization: $z_V = -0.40 \pm 1.30$. Apparently the charge division by the CDC sense wires is not perfectly simulated in the $GEANT$ algorithm.

The accuracies of determining the track parameters may also be estimated from a comparison with the input into the simulation. The comparison requires that the output of the tracking procedure is matched to the $GEANT$ input. This can only be achieved after specifying the limits in which the output has to agree with the input (matched tracks), i.e. the matching efficiency depends on the requested accuracies. There remains a certain percentage of reconstructed tracks which cannot be matched to the input (unmatched tracks) either because at least one of the characteristic track parameters p_t, φ, ϑ is outside the specified limit, or because the track is spurious. The matching and tracking efficiencies were studied in various modes, a few examples are presented in Table 1. The mode **a** corresponds to the tracking with the lc algorithm alone, the mode **b** also includes the cm algorithm with a $\Delta\vartheta$ range of 12°, the mode **c** is equivalent to mode **b** but with the $\Delta\vartheta$ range completely open, and the mode **d** is equivalent to mode **c** but with a narrow limit in the allowed hit deviation from the reconstructed track. The reduced efficiency in mode **a** is enforced by the initialization of the tracking parameters since the lc algorithm is only the first step of the complete tracking procedure. The sum of matched and unmatched tracks in Table 1 exceeds in most cases 100% which is a clear indication that, depending on the tracking mode, a 5% to 30% contribution of spurious tracks is contained in the simulated event sample. The amount of spurious tracks is reduced when a lower p_t cut of 100 MeV/c is applied. This was to be expected since pions with momenta below this limit start to curl in the CDC. They become ambiguous with respect to the π^- to π^+ separation and are very often assigned to both pions. The Table 1 lists in its lowest box the standard deviations of the matched tracks with respect to the parameters p_t, φ, ϑ. The p_t resolution is momentum dependent, the dependence is shown in Fig. 2. For low momenta $p_t < 0.5$ GeV/c the resolution is $\sigma_{p_t}/p_t = 0.04$ and then increases to 0.12 for transverse momenta close to 2 GeV/c. The standard deviations listed in Table 1 and shown in Fig. 2 should be considered as representative for the experimental resolutions, in case of σ_ϑ the value agrees very well with the resolution deduced in Subsect. 2.2 from the measured tracks.

The Table 1 demonstrates that the tracking efficiency with method I which includes the lc and cm algorithms, is more than 90%, and that there is a 10% probability for spurious tracks with transverse momenta $p_t > 100$ MeV/c. For smaller momenta this probability may increase to 20%. It should be pointed out that these conclusions depend only little on the track multiplicity. Of course they are based on the assumption that the $IQMD/GEANT$ calculations provide a representative simulation of the CDC behaviour. But there exist additional and alternative ways to test the quality of the tracking methods which were discussed in Subsect. 2.2.

2.4 Extrapolation to 4π solid angle

Although the $FOPI$ detector is meant to be a 4π detector this goal was only reached after the completion of the detector. With only the CDC and forward plastic-scintillator detectors present the pion identification was at that moment restricted to $150^\circ > \vartheta > 30^\circ$. The influence of these geometrical boundaries onto the acceptance of the CDC is displayed in Fig. 5. Also shown as shaded contours are the distributions of pions with momenta P less than $0.2, 0.4, 0.6$ GeV/c, and the upper momentum limit $p < 0.65$ GeV/c which is effective only for π^+. In general the $\vartheta < 150^\circ$ boundary does

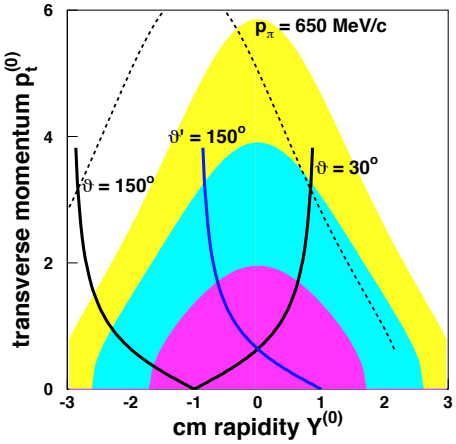

Fig. 5. The loci of the CDC geometrical limits $\vartheta = 30°$ and $\vartheta = 150°$ in the $p_t^{(0)}$ versus $Y^{(0)}$ plane of pions. Also shown is the $\vartheta' = 150°$ limit and, as *dotted curve*, the position of pions with laboratory momentum $p = 0.65$ GeV/c. The *shaded areas* correspond to pions with cm momenta $P < 0.2$, 0.4, 0.6 GeV/c

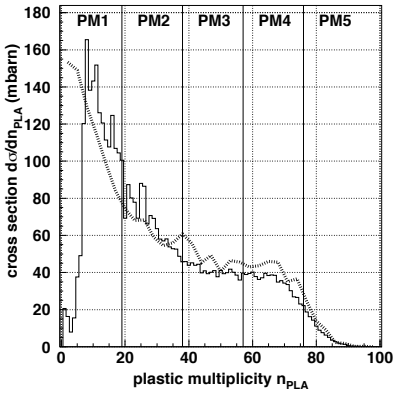

Fig. 6. Measured (*histogram*) and simulated (*dotted curve*) multiplicity distributions of particles measured with the PLA forward detector. The *vertical lines* define the 5 multiplicity bins $PM1$ to $PM5$ used in the text

Table 2. Partial reaction cross sections and impact parameters derived from the different multiplicity bins of the forward detector PLA

	σ (barn)	$b_{\min}$ (fm)	$b_{\max}$ (fm)	$< b_{\text{geo}} >$ (fm)	$< b_{\text{IQMD}} >$ (fm)
PM1cor	2.511	9.50	13.00	11.34	
PM1	1.674	9.50	11.95	10.77	11.23
PM2	1.299	7.03	9.50	8.33	8.55
PM3	0.784	4.98	7.03	6.06	6.49
PM4	0.670	1.93	4.98	3.68	3.93
PM5	0.119	0.00	1.93	1.29	2.77
PM5D1	0.047	0.00	1.22	0.81	1.71

not constitute a major problem since the pion emission into larger angles is very weak. The 30° cut, on the other hand, reduces the pion detection efficiency to approximately 65%.

Since in the reaction Au on Au target and projectile are identical this requires the existence of the following symmetry relation in the cm system:

$$f(\Theta, \Phi) = f(\pi - \Theta, \pi + \Phi) \quad (1)$$

where f is any angle dependent observable and $\Theta, \Phi = \varphi$ refer to the cm system. The validity of this relation can be tested since the $\vartheta > 30°$ cut extends into the forward hemisphere of the cm system. The test asks for the introduction of an additional angular cut $\vartheta' < 150°$ which is also shown in Fig. 5. The experimental data with $\vartheta > 30° \wedge \vartheta' < 150°$ should be symmetric around $Y^{(0)} = 0$, when projected onto the rapidity axis. With this condition on the polar angle the experimental data for π^- and π^+ have an asymmetry around $Y^{(0)} = 0$ of approximately 15%. The reason for this asymmetry is most likely due to the trapezoidal shape of the CDC. The signals on the outer wires for minimum ionizing tracks close to the cone have a large probability to disappear below the threshold of the FADC system. This leads to a systematic offset in the z vertex of these tracks and their deduced polar angles. The symmetry of the data therefore has to be imposed by applying the Eq. (1). This operation was either performed on the complete data sample or alternatively only on the data with $Y^{(0)} < 0$. The difference between both symmetrization procedures was added to the systematic error.

The data symmetrization also has the advantage that the effective solid angle for pions is now close to 4π. From the $IQMD$+$GEANT$ simulations one obtains a remaining inefficiency of $10 \pm 3\%$ for π^- and π^+ which is mainly due to the residual influence of the $\vartheta > 30°$ cut and the target shadow. In case of the pion multiplicities a 10% correction was applied, in all other cases the data remained uncorrected.

3 Experimental results

3.1 Charged particle multiplicities

The analyzed data are dominated by high-multiplicity events since the trigger conditions favored PLA multiplicities in the range 3 (c.f. Subsect. 2.1). The chosen scale-down factors were used to generate a corrected multiplicity spectrum of the PLA detector which is shown in Fig. 6. In this spectrum the estimated background contribution from non-target reactions was subtracted. The scale-down corrections are applied to all results of this section, they thus correspond to the 'minimum bias' condition. It has become common practice [44] to divide the complete multiplicity range into 5 bins PM, where the lower limit of the fifth bin $PM5$ is defined as the multiplicity of half the plateau value. The four lower bins have equal widths. The boundaries of $PM1$ to $PM5$ are displayed in Fig. 6.

Using the information from the beam counter, the dead time corrections of the data acquisition system, and the target thickness the reaction cross sections were calculated for each of the PM bins . These cross sections are listed in Table 2. Integrating over the complete multiplicity range one derives a total cross section $\sigma_{\text{reac}} = 4.546$ barns. However the Fig. 6 clearly indicates that the PLA multiplicity distribution in the lowest bin $PM1$ is cut at values $n_{\text{PLA}} < 8$. A likely reason is that for such low-multiplicity reactions the majority of particles is emitted into angles $\vartheta < 7°$ which is the lower acceptance angle of the PLA detector. Although there exists an additional detector, the zero degree detector ZER [25], at smaller angles $1.2° < \vartheta < 7°$, the PLA trigger condition prohibits the readout at smaller multiplicities. The magnitude of the missing cross section is estimated to be of half the

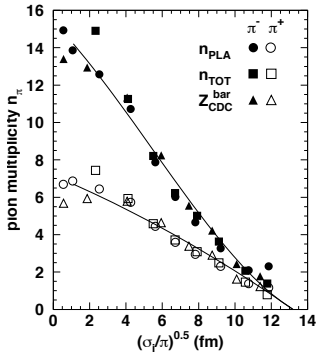

Fig. 7. Measured charged pion multiplicities as function of the integrated cross section deduced from the forward particle multiplicity $n_{\rm PLA}$, the total particle multiplicity $n_{\rm TOT}$,and the Baryonic charge $Z_{\rm CDC}^{\rm bar}$ (see text)

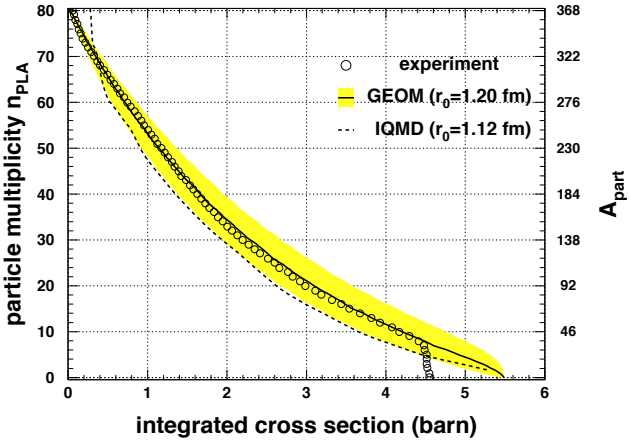

Fig. 8. The *open circles* show the measured cross sections as function of the forward particle multiplicity $n_{\rm PLA}$. The *full curve* shows the cross section as functions of the number of participants $A_{\rm part}$ obtained from the geometrical model with smooth surface. The *shaded area* corresponds to an uncertainty of the surface parameter $a = 1 \pm 0.6$ fm (see text). The *dotted curve* is the prediction of the $IQMD$ model

size of the measured cross section in the $PM1$ bin. If this loss is taken into account the total cross section increases to $\sigma_{\rm reac} = 5.5 \pm 0.5$ barns.

In Fig. 6 the measured cross section $\frac{d\sigma}{dx}$ is shown as a function of $x = n_{\rm PLA}$. The cross section can also be determined for other measured variables like the total multiplicity $n_{\rm TOT}$ measured with the PLA and CDC, or the baryonic charge $Z_{\rm CDC}^{\rm bar}$ measured with the CDC. In all three cases the charged pion multiplicities n_{π^-}, n_{π^+} increase with increasing values of x. The measured cross sections $\frac{d\sigma}{dx}$ allow to display this common behaviour as function of a unified variable, i.e. the integrated cross section [37]

$$\sigma_i = \int_{x_{\rm max}}^{x_i} \frac{{\rm d}\sigma}{{\rm d}x} {\rm d}x = \sigma(x_i) \tag{2}$$

since $\sigma(x_{\rm max}) = 0$. In Fig. 7 n_{π^-} and n_{π^+} are shown as functions of $\sqrt{\sigma_i/\pi}$ with $x = n_{\rm PLA}, n_{\rm TOT}, Z_{\rm CDC}^{\rm bar}$. The curves in Fig. 7 are fits to the measured data by a third order polynomial, where it is assumed that $n_\pi = 0$ for $\sigma_i = \sigma_{\rm reac}$.

Although σ_i is a unified variable it is more common to present the pion multiplicities as functions of the number of participants $A_{\rm part}$. The values of $A_{\rm part}$ depend on the size of σ_i, they can be obtained from the comparison with the geometrical cross section

$$\sigma_{\rm geo}(b) = 2\pi \int_0^b \rho^2(r/2) r \, {\rm d}r / \rho_0^2. \tag{3}$$

In order to relate $A_{\rm part}$ to x via the equality $\sigma_{\rm geo}(b) = \sigma(x_i)$ the variable x has to be a monotonous function of b, i.e. an increase in x has to correspond to a decrease in b. The nuclear density profile $\rho(r)$ was parametrized by the Fermi form

$$\rho(r) = \rho_0 (1 + \exp\{(r - r_0)/a\})^{-1} \tag{4}$$

where from electron scattering [45] the nuclear radius is $r_0 = 1.2 \cdot A^{1/3}$ fm. This choice and the total cross section $\sigma_{\rm reac} = 5.5 \pm 0.5$ barns determine the surface parameter a to be $a = 0.4 \pm 0.3$ fm. Notice that the sharp surface model with $a = 0$ fm would require a nuclear radius $r_0 = (1.14 \pm 0.05) \cdot A^{1/3}$ fm to yield the measured value of $\sigma_{\rm reac}$. The average impact parameters for the different PM bins calculated with the sharp surface approximation are listed in Table 2. Except for the $PM1$ bin these values do not change with the smooth surface approximation, for this first bin the impact parameter increases with this approximation by 5%.

However, both models completely ignore the fluctuations in the measured particle multiplicities $n_{\rm PLA}$. These fluctuations have a severe effect on the extracted impact parameters for near-central collisions. The size of the effect can be estimated when the collision is studied with a dynamic model like the $IQMD$ model where $n_{\rm PLA}$ for every event fluctuates around a mean for a given impact parameter b. In the present realization of the $IQMD$ model the colliding nuclei are described by sharp spheres with a radius $r_0 = 1.12 \cdot A^{1/3}$ fm which corresponds to a total cross section $\sigma_{\rm IQMD} = 5.34$ barns. The relation between cross section and impact parameter b obtained from the $IQMD$ model is also shown in Table 2. From the cross section of the $PM5$ bin the impact parameter cannot be deduced to an accuracy better than $b < 3$ fm. To improve the selection of central events additional criteria have to be imposed. The one used here is the degree of azimuthal isotropy expressed by the directivity [36, 38]

$$D = |\sum w \mathbf{p_t}| / \sum |\mathbf{p_t}|, \tag{5}$$

where $w = 1$ for $Y^{(0)} > 0$ and $w = -1$ for $y_{\rm cm}^{(0)} < 0$. Contrary to previous $FOPI$ publications the summation now includes all registered particles from the PLA and the CDC detectors. Truely isotropic events should have a directivity $D = 0$. Because of the finite particle numbers the directivity distribution is of Poisson form with a mean value inversely proportional to the square root of the particle multiplicity. In general $0 \leq D \leq 1$. In order to select more-central events the $PM5$ criterion was supplemented by a $D1$ criterion which implies $D < 0.15$. This reduces the cross section for the $PM5D1$ bin to 47 mbarns, the corresponding impact parameters calculated with the sharp surface model are listed in Table 2.

With the impact parameter b known the number of participating nucleons $A_{\rm part}$ can be calculated from the geometrical overlap of the colliding nuclei and their nuclear density

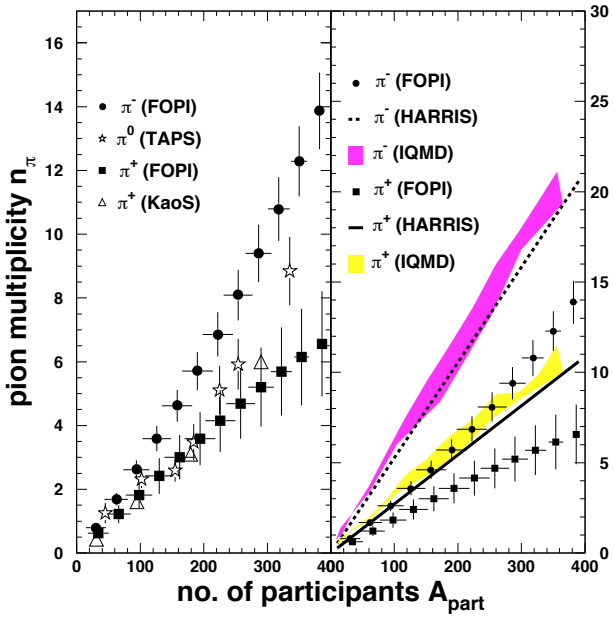

Fig. 9. *Left:* Comparison of the measured π^- and π^+ multiplicities with the corresponding results of $TAPS$ and $KaoS$. *Right:* Comparison of the measured π^- (*circles*) and π^+ (*squares*) multiplicities with the results of $IQMD-GEANT$ simulations and the extrapolation of Harris et al.

profile $\rho(r)$:

$$A_{\text{part}}(b) = 2 \int_0^{r_{\max}} \rho(r)\Theta(r_{\max}^2 - (x^2+y^2+z^2)) \times \Theta\,(r_{\max}^2 - ((b-x)^2+y^2)\,\mathrm{d}x\,\mathrm{d}y\,\mathrm{d}z. \quad (6)$$

Compared to the results of electron scattering [45] the surface parameter $a = 0.4 \pm 0.3$ fm, needed to reproduce the total cross section σ_{reac}, is too small. We have used instead for the calculation of A_{part} a value $a = 1.0 \pm 0.6$ fm which includes as the lower limit the value from the total cross section but is more in line with electron scattering. The upper integration limit is defined by $r_{\max} = r_0 + a$. The uncertainty in a is also used to estimate the error of A_{part} as determined by the present method. Figure 8 displays the relation between $x = n_{\text{PLA}}$ and A_{part} by using either the smooth surface model as described above, or the $IQMD$ model with a surface parameter $a = 0$ fm. Figure 8 indicates that the smooth surface approximation is closer to the measured $\sigma_{\text{exp}}(n_{\text{PLA}})$ than the $IQMD$ model. The relative error of A_{part} decreases with increasing A_{part}, for near-central collisions the $IQMD$ model confirms the expected insensitivity of the measured cross section to A_{part}.

Besides n_{PLA} also the other observables n_{TOT} and $Z_{\text{CDC}}^{\text{bar}}$ were employed to determine A_{part} by the same method. Since these observables cover different parts of the phase space and since they contain different particle types (e.g. $Z_{\text{CDC}}^{\text{bar}}$ does not include charged pions whereas n_{PLA} and n_{TOT} do) the extracted dependence of the charged pion multiplicities on A_{part}, discussed in the next paragraph, incorporate effects due to the uncertain participant-spectator separation or self correlations.

The measured charged pion multiplicities n_{π^-} and n_{π^+} in 4π solid angle increase with increasing A_{part}, the increase is not completely linear. The dependence on A_{part} was therefore fitted to a potential expansion in A_{part}, i.e.

$$n_\pi = a_1^{(3)} \cdot A_{\text{part}} + a_2^{(3)} \cdot A_{\text{part}}^2 + a_3^{(3)} \cdot A_{\text{part}}^3, \quad (7)$$

where the upper index (3) indicates the degree of the expansion. We found no systematic dependence of $a_1^{(3)}$, $a_2^{(3)}$, $a_3^{(3)}$ on the choice of x, the values for π^- are
$a_1^{(3)} = (2.621 \pm 0.094)10^{-2}, a_2^{(3)} = (1.377 \pm 0.569)10^{-5}$,
$a_3^{(3)} = (3.311 \pm 0.183)10^{-8}$,
and for π^+
$a_1^{(3)} = (1.824 \pm 0.135)10^{-2}, a_2^{(3)} = (5.675 \pm 1.416)10^{-6}$,
$a_3^{(3)} = (-2.304 \pm 0.121)10^{-8}$.
Only the systematic errors are quoted, the uncertainty in these fit parameters was used to calculate the error of n_π. The dependence of n_{π^-} and n_{π^+} on A_{part}, as obtained from (7), is displayed in Fig. 9. Figure 9 also shows the results for π^+ obtained by the $KaoS$ collaboration [46], and for π^0 obtained by the $TAPS$ collaboration [34]. In case of π^+ the agreement between the two different experiments seems quite satisfactory. Notice, however, that the $KaoS$ and also the $TAPS$ results were measured within a relatively small solid angle, the extrapolation into 4π solid angle requires the application of a model to describe the phase space distribution of pions. Both collaborations have used the model of a thermal pion source located at $Y^{(0)} = 0$, and the extrapolation therefore depends on the correctness of this model. The Subsects. 3.2.2, 3.2.3, and 3.2.4 will present convincing evidence that rescattering phenomena in the spectator matter destroy the angular isotropy of the pion emission and the apparent pion temperatures. But since charged pions are detected by the present experiment in almost complete phase space the error made by extrapolating from the midrapidity region into 4π can be estimated. This extrapolation underpredicts the charged pion cross sections by a factor 0.87 ± 0.05.

The obvious conclusion from Fig. 9 is that the π^- multiplicity is always larger than the π^+ multiplicity. For both pion charges the increase of the experimental pion multiplicities with A_{part} deviates from a purely linear dependence. Even the π^- to π^+ ratio is not constant with A_{part} but increases with rising values of A_{part}. Notice that these dependencies will not disappear when A_{part} is determined by a different method. In case the measured multiplicities are fitted by a linear expansion $n_\pi = a_1^{(1)} \cdot A_{\text{part}}$, the π^- to π^+ ratio is determined to $R_\pi = a_1^{(1)}(\pi^-)/a_1^{(1)}(\pi^+) = 1.95 \pm 0.04 \pm 0.30$. This value is in perfect agreement with the prediction $R_\pi = 1.95$ from the isobaryonic model [7]. On the other hand the inspection of Fig. 9 reveals that the quoted value of R_π is mainly determined by the pion multiplicities at large values of A_{part}. For these values the differential cross section $d\sigma/dA_{\text{part}}$ approaches a minimum. The dependence of A_{part} on the impact parameter b is almost Gaussian in the geometrical model Eq. (6). Using this dependence it is easy to derive that

$$d\sigma/dA_{\text{part}} = \sigma_0/A_{\text{part}} \quad (8)$$

where σ_0 is a cross section that depends on the width of the Gaussian and will later cancel out. With the help of (7) and (8) one obtains the average number of charged pions per A_{part}

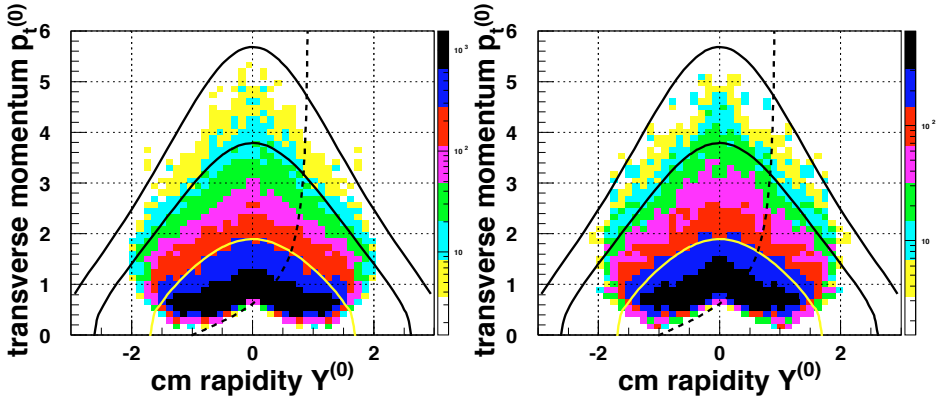

Fig. 10. The *left panel* shows the distribution of negative pions in the $p_t^{(0)}$ versus $Y^{(0)}$ plane as logarithmic contours, the *right panel* shows the same for positive pions. The *full curves* correspond to pions with cm momenta P = 0.2, 0.4, 0.6 GeV/c, the *dotted curves* display the geometrical limit $\vartheta = 30°$ of the CDC

$$\frac{< n_\pi >}{< A_{\rm part} >} = \frac{\int n_\pi \frac{{\rm d}\sigma}{{\rm d}A_{\rm part}} {\rm d}A_{\rm part}}{\int A_{\rm part} \frac{{\rm d}\sigma}{{\rm d}A_{\rm part}} {\rm d}A_{\rm part}}$$
$$= a_1^{(3)} + \frac{a_2^{(3)}}{2} \cdot A_0 + \frac{a_3^{(3)}}{3} \cdot A_0^2 \qquad (9)$$

where $A_0 = A_P + A_T$. This yields for negative and positive pions

$$\frac{< n_{\pi^-} >}{< A_{\rm part} >} = (3.08 \pm 0.04 \pm 0.37) \cdot 10^{-2}$$
$$\frac{< n_{\pi^+} >}{< A_{\rm part} >} = (1.82 \pm 0.09 \pm 0.43) \cdot 10^{-2}$$

and for the average π^- to π^+ ratio $< R_\pi >= 1.69 \pm 0.09 \pm 0.26$ where we assume that systematic errors change the nominator and denominator of R_π in the same direction. The observed nonlinearities of n_{π^-} and n_{π^+} with $A_{\rm part}$ and also other dependencies which shall be discussed later clearly indicate that the difference between the π^- and π^+ production is not only the result of isospin conservation and a ratio $N/Z > 1$.

3.2 The phase space distributions of charged pions

The invariant and symmetrized cross sections $1/2\pi p_t \cdot d^2\sigma / dp_t dy$ for π^- and π^+ are displayed in Fig. 10 as contours of decreasing grey shades. The depth of the shade decreases with the logarithm of the cross section, the units on the right-hand scales correspond to μbarn(MeV/c)$^{-2}$. Figure 10 also displays as full curves the invariant cross sections of charged pions with momenta 0.2, 0.4, 0.6 GeV/c emitted from a thermal source at $Y^{(0)} = 0$. Also shown as dotted curve is the forward CDC boundary at $\vartheta = 30°$. The data on the right side of this curve are therefore not measured but were generated by applying (1).

The measured cross sections in Fig. 10 vary only weakly with particle or pion multiplicity, they are therefore shown under 'minimum bias' condition. The comparison with the thermal curves reveals that the patterns of the π^- and π^+ cross sections do not fully agree with the hypothesis of thermal emission from the central fireball. The longitudinal deviation from the thermal emission pattern was also observed in light-mass systems [7]. For a more detailed analysis the invariant cross sections shown in Fig. 10 will be mapped into specific quantities as presented in the next subsections.

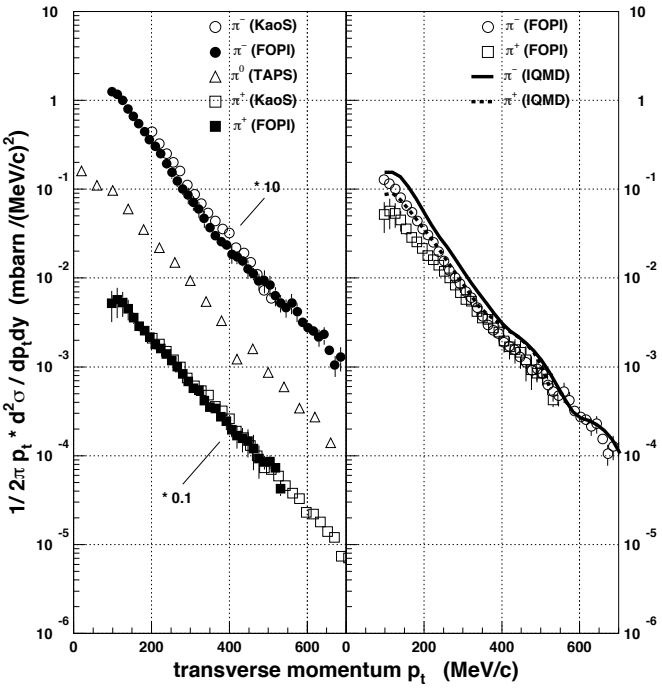

Fig. 11. *Left:* Comparison of the measured pion transverse momentum distributions at midrapidity with the corresponding results of $TAPS$ and $KaoS$. *Right:* Comparison of the measured pion transverse momentum distributions at midrapidity with the results of $IQMD - GEANT$ simulations. The cross sections are normalized to a rapidity interval dy = 1

The interpretation of the resulting distributions will be first attempted by assuming the existence of a thermalized pion source at midrapidity $Y^{(0)} = 0$. The validity of this assumption requests a unique pion temperature and an isotropic pion angular distributions in the fireball frame. Both requirements are violated. It will become evident that the picture of a central source has to be modified because the remnants from the target and projectile disturb the emission pattern of pions from the central source. Furthermore pions are at least partially produced by the decay of Baryon(S=0) resonances which leave their imprint on the shape of the pion energy distributions.

3.2.1 Transverse momenta. In order to obtain the transverse momentum distributions of charged pions under 'minimum bias' condition a range in rapidity $-0.2 < Y^{(0)} < 0.2$ was defined. Only pion data in this range, but normalized

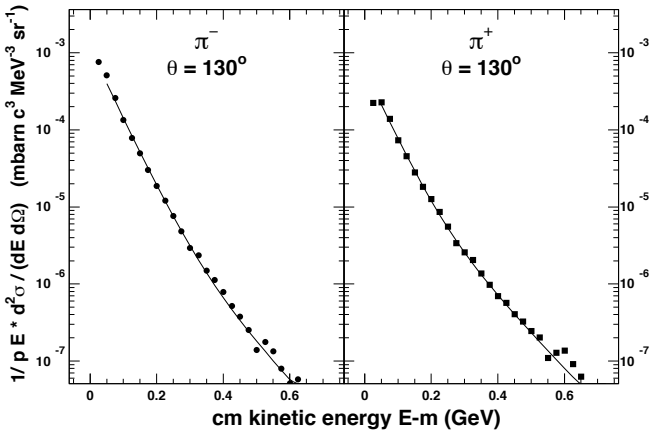

Fig. 12. Measured cm kinetic energy distributions of pions at cm angle $\Theta = 130°$. The curves display the corresponding two-temperature fits using angle averaged temperatures

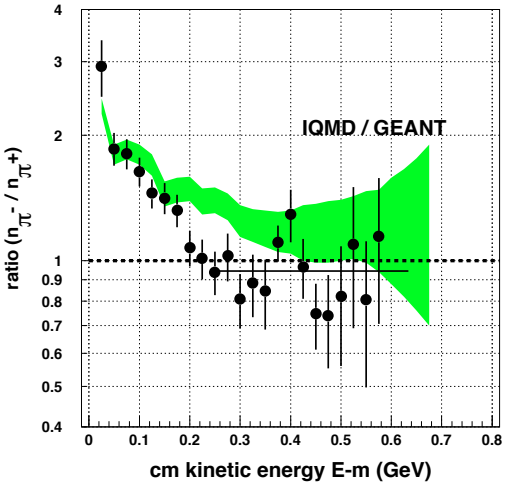

Fig. 13. Kinetic energy dependence of the measured π^-/π^+ ratio. The *full line* corresponds to a π^- to π^+ ratio of 0.93. The *shaded area* shows the $IQMD$ prediction

to $dy = 1$, were used to obtain the invariant cross section $1/2\pi p_t \cdot d^2\sigma/dp_t dy$ which is shown in Fig. 11 for π^- and π^+. For reasons of comparison this Fig. 11 also includes similar results from the $KaoS$ [29] and $TAPS$ [32, 34] collaborations, where the respective rapidity ranges are $-0.25 < Y^{(0)} < 0.21$ ($TAPS$) and $-0.20 < Y^{(0)} < 0.47$ ($KaoS$, the boundaries depend on $p_t^{(0)}$). The agreement between comparable experiments is very good. The lower limit of the $FOPI$ results at $p_t = 0.1$ GeV/c is mainly due to the $\vartheta > 30°$ cut. In addition this limit was also imposed to eliminate the region where the number of spurious tracks is particularly large. That the π^+ distribution does not extend beyond $p_t > 0.5$ GeV/c is due to the limitation $p < 0.65$ GeV/c which is necessary to separate p from π^+. After the completion of the $FOPI$ detector this limit will be pushed to $p < 1$ GeV/c since the particle velocity will also be measured. For the interpretation of the pion spectra in terms of a thermalized source it is more convenient to study the pion kinetic energies at selected emission angles. The p limitation for the π^+ restricts the kinetic energy at $\Theta = 90°$ to $E - m < 0.4$ GeV, the limit increases with angle and reaches $E - m < 0.6$ GeV at $\Theta = 120°$.

3.2.2 Kinetic energies. The differential cross sections $F_\pi(E) = 1/PE \cdot d^2\sigma/dEd\Omega$ were obtained under 'minimum bias' condition in the backward hemisphere of the cm system in 10° steps with a width of ±5°. For the cm angle $\Theta = 130°$ and for π^- and π^+ the kinetic energy spectra are displayed in Fig. 12. Assuming the emission from a thermalized source at midrapidity one expects $F_\pi(E)$ to decrease exponentially like $C_\pi \cdot \exp(-E/T)$ where the inverse slope parameter is the temperature T. It was observed before [29] and can also be seen in Fig. 12 that this expectation is not supported by the data. Rather the π^- and π^+ kinetic energy spectra have concave shapes which require the assumption of at least 2 temperatures if the spectra are to be fitted by the superposition of exponentials, i.e. $F_\pi(E)$ is of the form

$$F_\pi(E) = C_{\mathrm{l},\pi} \cdot \exp(-E/T_{\mathrm{l},\pi}) + C_{\mathrm{h},\pi} \cdot \exp(-E/T_{\mathrm{h},\pi}) \quad (10)$$

with $C_{\mathrm{l},\pi}, C_{\mathrm{h},\pi}, T_{\mathrm{l},\pi}, T_{\mathrm{h},\pi}$ as independent parameters. In the present analysis the π^- kinetic energy spectra were fitted in the range between 0.05 and 0.75 GeV, for the π^+ the upper limit changed with Θ between 0.4 and 0.75 GeV. The results of these fits are also shown in Fig. 12. It is evident that at small energies the slope of the π^- spectrum is different from that of the π^+ spectrum. This is clearly demonstrated by the ratio $R_E = F_{\pi^-}(E)/F_{\pi^+}(E)$ which is displayed in Fig. 13. For reasons discussed later only the data from the angular range $85° < \Theta < 135°$ are included. Obviously the ratio has a maximum value $R_E = 3$ for the smallest measured kinetic energy $E - m = 0.025$ GeV and then decreases with increasing energy to values close to $R_E = 1$ for energies $E - m > 0.3$ GeV. The first point is shown despite the systematic errors in the pion identification because the ratio should be less effected by those errors. Since the slope of the π^- and π^+ spectra appears to be the same for large kinetic energies it was assumed that the high π^- temperature is equal to the high π^+ temperature for all Θ angles. The extension to angles $\Theta > 135°$ was made although for these angles the π^+ spectra at large kinetic energy are not well reproduced by a thermal Maxwell-Boltzmann distribution with two temperatures.

The temperatures deduced from the two-temperature fits, i.e. the low temperatures $T_{\mathrm{l},\pi}$ and the high temperature $T_{\mathrm{h},\pi}$ change with angle Θ. The angle dependence is displayed in Fig. 14. The errors are mainly systematic, i.e. they indicate the differences from the three different tracking analyses. In addition the temperatures will also change when the energy range used for the fit is changed. This uncertainty is not included in the error. The variation with emission angle Θ is largest for the high temperature, this temperature increases by a factor 2 at $\Theta = 150°$. At angles $\Theta > 135°$ also the pion angular distributions are enhanced, this will be shown in the next subsection. We have therefore selected an angular range $\Theta < 135°$ and have deduced from Fig. 14 average temperatures in this range for pions emitted from the central source. The average low temperature for π^- is $T_{\mathrm{l},\pi^-} = 42.2 \pm 2.7 \pm 2.2$ MeV, for π^+ one obtains $T_{\mathrm{l},\pi^+} = 49.4 \pm 2.3 \pm 3.7$ MeV. The common average high temperature for π^- and π^+ is $T_{\mathrm{h},\pi} = 96.4 \pm 5.1 \pm 4.5$ MeV.

The fact that the pion temperatures do not change very much for angles $|90° - \Theta| < 45°$ can be taken as evidence

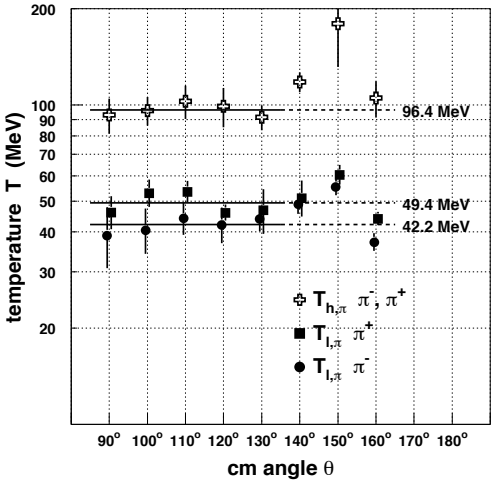

Fig. 14. Angular dependence of the inverse slope parameters $T_{\mathrm{l},\pi}, T_{\mathrm{h},\pi}$ of a two-temperature fit to the kinetic energy spectra of π^- and π^+. The lines show the averaged temperatures for $85° < \Theta < 135°$

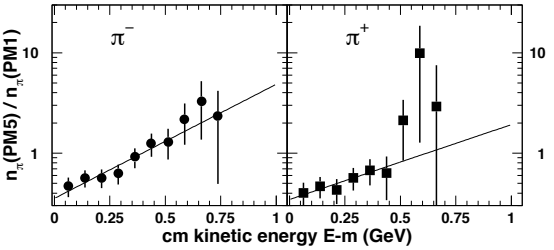

Fig. 15. Ratio of the kinetic energy spectra for peripheral($PM1$) to central ($PM5$) reactions for π^- and π^+. The *full lines* are exponential fits to the data points

that at least for these angles the contribution of pions from sources other than the central source is weak. The reason for the concave shapes of their energy spectra is therefore not caused by multiple sources but due to a different mechanism. Most likely the shape reflects the decay of Baryon resonances [46]. In this case the concept of two temperatures appears artificial and it should be considered as only a method to parametrize the pion energy spectra. Nevertheless this parametrization is necessary to calculate the pion rapidity spectra that one expects from a central source with this type of energy distributions. For this purpose the contribution of the low-temperature component $I_{\mathrm{l},\pi}$ to the total pion yield $I_\pi = I_{\mathrm{l},\pi} + I_{\mathrm{h},\pi}$ has to be known. The yields for π^- and π^+ were obtained by integrating $d^2\sigma/dEd\Omega$ over the energy and the angular range $85° < \Theta < 135°$. The results are $I_{\mathrm{l},\pi^-}/I_{\pi^-} = 0.43 \pm 0.04 \pm 0.16$ and $I_{\mathrm{l},\pi^+}/I_{\pi^+} = 0.43 \pm 0.03 \pm 0.25$, i.e. the high-temperature component is for both charged pions under the present conditions comparable to the low-temperature component.

On the other hand at angles $\Theta > 135°$ the pion temperatures and also the angular distributions, discussed in the next subsection, suggest the possibility that pions are not only emitted from a source at midrapidity, but that secondary sources exist which contribute to the pion yield at very backward (and forward) angles. In order to study at least qualitatively the nature of these sources we have fixed their location at $Y^{(0)} = \pm 1$ and have reanalized the pion kinetic energy spectra in the target frame. These spectra have, similar to the ones in the fireball frame, concave shapes. For angles $\vartheta > 85°$ the low and high temperatures first decrease with increasing angle and then become reasonably constant within their error limits for $\vartheta > 105°$. The average low temperatures in the range $105° < \vartheta < 135°$ are $T_{\mathrm{l},\pi^-} = 25.1 \pm 4.5 \pm 6.3$ MeV and $T_{\mathrm{l},\pi^+} = 31.8 \pm 6.5 \pm 11.2$ MeV. Thus the low pion temperatures of this hypothetical source at target rapidity are approximately 15 MeV smaller than deduced for the central source. But, of course, these sources are not well separated in rapidity space (c.f. Sect. 3.2.4), and the reduction of the extracted temperatures should only be taken as evidence that the secondary sources are cooler, as one might have expected.

Finally we have studied whether or not the pion kinetic energy distributions change with impact parameter, i.e. with the measured multiplicity in the PLA detector. For this purpose, peripheral reactions were selected by considering only the data of the $PM1$ multiplicity bin, similarly central reactions were defined by the $PM5$ bin. The energy spectra for $PM5$ in the angular range $85° < \Theta < 135°$ were divided by those for $PM1$, the results for π^- and π^+ are displayed in Fig. 15. It is evident that there is a systematic decrease of the pion temperatures for peripheral reactions, respectively an increase for central reactions. Furthermore, for π^- and π^+ the increase seems to occur particularly at large kinetic energies. However, within the estimated errors this difference is not significant. Assuming therefore an energy independent increase of the temperature with particle multiplicity, one finds this increase to be small. For π^- it amounts to $\Delta T = 5.2 \pm 2.5$ MeV and for π^+ to $\Delta T = 4.4 \pm 2.5$ MeV. The quoted errors were obtained from the enhanced background of $PM1$ events, systematic errors were not deduced in this case. Thus temperature changes are observed but they are not larger than the accuracy to determine the temperature values. A similar result was obtained by the $KaoS$ collaboration [29].

3.2.3 Angular distributions. The inconsistency of a pure thermal approach to pion production is also seen in their polar angular distributions in the fireball frame. Under 'minimum bias' condition and for both pion charges these angular distributions are anisotropic with a strong increase of the cross section $d\sigma/d\Omega$ for forward and backward angles, see Fig. 16. Within the angular range $45° < \Theta < 135°$ the cross section is almost constant, a behaviour which is reminescent of the angular variations of the pion temperatures. The isotropy of $d\sigma/d\Omega$ in this angular range depends, however, on the pion energy. The angular distributions shown in Fig. 16 were obtained including all kinetic energies with $E - m > 40$ MeV. When this lower cut-off is raised to $E - m > 365$ MeV the resulting angular distribution of the π^- develops an additional maximum at $\Theta = 90°$, i.e. high-energetic negative pions have a preference to be emitted vertically to the beam axis at midrapidity. Because of the momentum cut $p < 0.65$ GeV/c applied to the π^+ it is not possible to confirm that positive pions display a similar behaviour.

It should be noted that the forward-backward enhancement in the pion angular distributions does not vanish when central, i.e. $PM5$ collisions with $E - m > 40$ MeV are

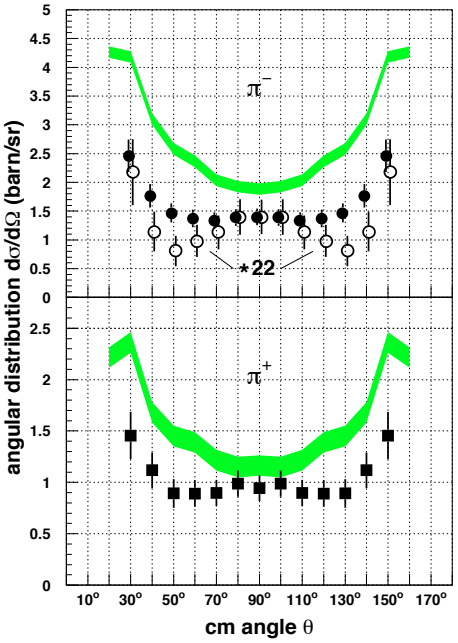

Fig. 16. Measured (*circles*, *squares*) and simulated (*shaded areas*) angular distributions of π^- and π^+. *Full symbols* correspond to pion energies $E - m > 40$ MeV, *open symbols* to $E - m > 365$ MeV

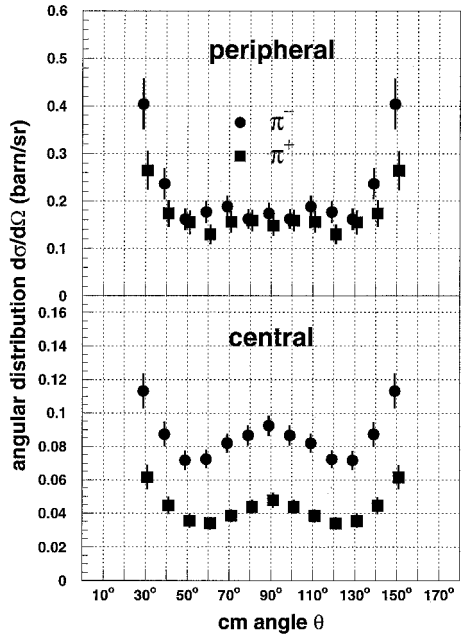

Fig. 17. Measured angular distributions of charged pions from peripheral ($PM1$, *top*) and central ($PM5$, *bottom*) collisions

selected. On the other hand there exist differences in the pion angular distributions of peripheral ($PM1$) and central ($PM5$) collisions. These differences are most pronounced at at $\Theta = 90°$, where the angular distribution for central collisions displays a secondary maximum which is not seen for peripheral collisions, see Fig. 17. For a quantitative comparison peripheral and central collisions were normalized at forward, respectively backward angles, and the midrapidity enhancement was calculated by means of the ratios $\frac{d\sigma}{d\Omega}(90°, PM5)/\frac{d\sigma}{d\Omega}(90°, PM1) = 1.7 \pm 0.5$ for π^- and $\frac{d\sigma}{d\Omega}(90°, PM5)/\frac{d\sigma}{d\Omega}(90°, PM1) = 1.5 \pm 0.4$ for π^+, where all pions with $E - m > 40$ MeV are included. The midrapidity enhancement with peaking at $\Theta = 90°$ is apparently not observed in light-mass systems [7].

To conclude this subsection we point out that the enhanced emission into directions perpendicular to the beam momentum is found for high-energy pions under 'minimum bias' condition, and for pions of all energies from central collisions. Under all conditions pion emission into the directions close to the beam momentum is enhanced. Thus the topology of pion emission in nucleus-nucleus collisions is rather complex. Besides its dependence on the distribution of spectator matter it is probably also determined by the dynamical evolution of the fireball. The forward - backward enhancement of the pion yield is a phenomenon which was first found in the elementary pp reaction [47]. It is an open question whether this phenomenon could also be responsible for the present observation. The multitude of pion generations produced during the Au on Au reaction suggests that the memory on the original momentum direction in the entrance channel is effectively erased. It is therefore remarkable that the forward-backward enhancement depends so weakly on the impact parameter.

3.2.4 Rapidities. Different sources are usually distinguished and separated by their different cm velocities, i.e. in the relativistic case by their different rapidities. The rapidity distributions of charged pions were obtained after limiting the allowed p_t values to $p_t > 0.1$ GeV/c or $p_t^{(0)} > 1.0$. This lower p_t cut was introduced in order to avoid the rapidity dependence of the geometric CDC acceptance and to minimize the contribution of spurious tracks. From Fig. 10 it is evident that this cut has considerable influence onto the extracted rapidity distributions. For the 'minimum bias' condition these distributions for π^- and π^+ are displayed in Fig. 18. Note that the 3% background contribution from non-target reactions was neglected. As discussed in Subsect. 2.2 the background mainly effects events with very low multiplicity ($PM1$). The rapidity distributions of such background reactions can be obtained by shifting the z_V coordinate of the reaction vertex outside the acceptance range. Since this procedure simultaneously changes the origin of the reaction along the beam axis it is questionable, whether the extracted background rapidity spectra really represent the true background within the z_V acceptance. Background corrections were therefore, and because of their small size not applied.

It is evident from Fig. 18 that the measured rapidity spectra have nonthermal shapes. But they are also not consistent with the assumption of one central source with two different temperatures. In order to demonstrate this inconsistency more clearly Fig. 18 also shows, as dotted curves, the expected thermal distributions where the pion temperatures deduced in the preceeding subsection were used together with the extracted ratios between the low- and high-temperature components. For a given temperature the thermal rapidity distribution is nearly Gaussian, the correct expression was recently published by Schnedermann et al. [48]:

$$\frac{dn}{dY} = n_0\, T^3 \left(\frac{m_{t,0}^2}{T^2} + \frac{m_{t,0}}{T} \frac{2}{\cosh Y} + \frac{2}{\cosh^2 Y} \right)$$

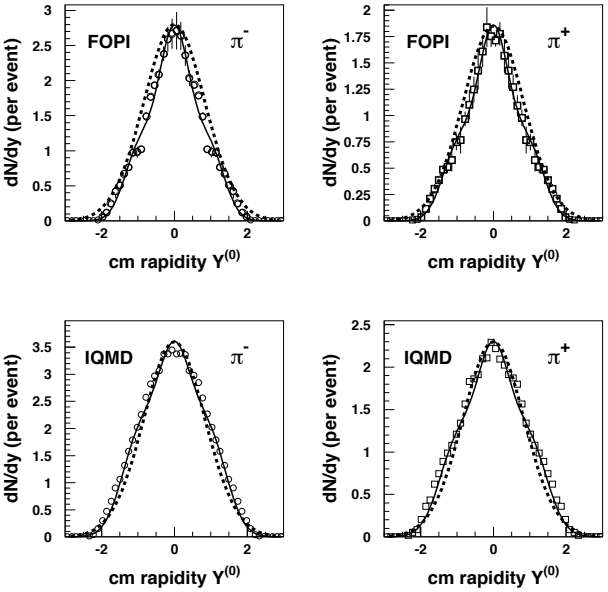

Fig. 18. Measured (*upper panels*) and simulated (*lower panels*) rapidity distributions of π^- and π^+ with transverse momenta $p_t^{(0)} > 1$. The *full curves* represent fits under the assumption of three pion sources (see text), the *dashed curves* represent the expected thermal distributions from the midrapidity source with temperatures $T_{\mathrm{l},\pi}$ and $T_{\mathrm{h},\pi}$

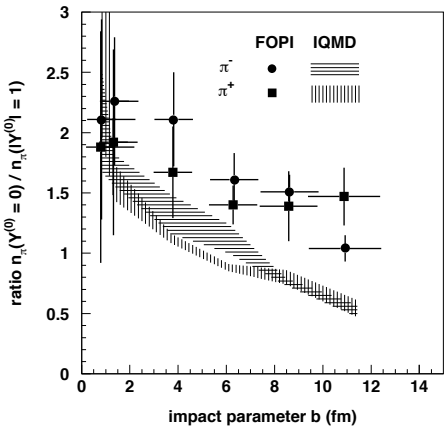

Fig. 19. Measured (*full symbols*) and simulated (*striped areas*) ratios of pions from the participant source to pions from the spectator sources as a function of impact parameter

$$\times \exp\left(-\frac{m_{\mathrm{t},0}}{T}\cosh Y\right), \tag{11}$$

where for $p_t > 0.1$ GeV/c one obtains $m_{\mathrm{t},0} = 172$ MeV, and the normalization constant n_0 is adjusted to the maximum of the measured distribution. Figure 18 suggests that the extrapolation from the midrapidity region into 4π overpredicts the total pion cross section, in variance with the opposite statement in Sect. 3.1. This contradiction is due to the $p_t > 0.1$ GeV/c cut which severely reduces the cross sections at forward and backward angles Θ, i.e. in regions where the cross section is experimentally found to increase.

The observed deviations between the experiment and the one-source hypothesis are not too surprising. It was pointed out before that the angular variations of the pion temperatures and of their cross sections demonstrate the importance of the pion absorption and reemission processes during the nuclear collision. These processes were first identified in theoretical calculations [1, 49], they are believed to be the reason for the observed 'flow' effects of pions with respect to the reaction plane [27, 31]. Here the pion rescattering on the cold spectator matter is of particular importance. And although the bulges in the rapidity distributions for $|Y^{(0)}| > 1$ are not a direct proof for the assumption that they are also caused by pion rescattering in spectator matter, the simultaneous observation of the forward/backward enhancement in the pion angular distributions makes this assumption very plausible. The measured distributions were therefore fitted by assuming three pion sources located at $Y^{(0)} = 0$ and $Y^{(0)} = -1, Y^{(0)} = +1$. The rapidity distributions of pions emitted by these sources were assumed to be of Gaussian shape, characterized by a total intensity $I_{0,\pi}, I_{1,\pi}$ and a width $\sigma_{0,\pi}, \sigma_{1,\pi}$. The assumption of Gaussian shapes is made because the correct shapes from rescattering processes by spectator matter are not known. But it is evident that a strong correlation between the central and the spectator sources must exist which will certainly modify the assumed thermal shapes. The results of the fits are shown as full curves in Fig. 18. These fits are not completely satisfactory. In both, the π^- and the π^+ rapidity distributions the pion yield is poorly reproduced at rapidity values $|Y^{(0)}| > 1$. This can have more than only one reason. For example, the sources might not be located only at $Y^{(0)} = \pm 1$, or the emission from the source might not be isotropic. The quality of the data does not allow to differentiate between the different possibilities. The three-source hypothesis should be regarded as only a first attempt to improve the picture over that of a central and thermal source. The values of the fit parameters $\sigma_{0,\pi}, \sigma_{1,\pi}$ and for the intensity ratio $R_{\mathrm{I},\pi} = I_{0,\pi}/(2 \cdot I_{1,\pi})$ are presented in Table 3.

In the geometrical model the size of the spectator matter changes with impact parameter b. It is therefore interesting to study the dependence of the intensity ratio $R_{\mathrm{I},\pi}$ and the widths $\sigma_{0,\pi}, \sigma_{1,\pi}$ on the PLA multiplicity. For each of the 5 multiplicity bins $PM1$ to $PM5$ and for $PM5D1$ the rapidity spectra were extracted and fitted under the three-source assumption. The results are listed in Table 3, the impact parameter dependence of $R_{\mathrm{I},\pi}$ is shown in Fig. 19.

Within the errors the central widths appear to be independent of the PLA multiplicity, and their values are close to $\sigma_\pi = 0.45$ independent of the pion charge or the pion source. Notice that this width when interpreted by the thermal model corresponds to a temperature of only 20 MeV. Correspondingly the width of the rapidity distribution from a central source with the temperature $T_{\mathrm{l},\pi}$ should have a larger value which is quoted in Table 3 under the label thermal. The differences between the 'longitudinal' temperature obtained from the analyses of the rapidity distributions, and the 'transversal' temperatures deduced from the kinetic energy spectra at $\Theta = 90°$ are further strong indications that the pion rescattering mechanism cannot be described by a thermal parametrization. As seen in Fig. 19 and Table 3 the measured ratio $R_{\mathrm{I},\pi}$ is always larger than one. This proofs that the main contributor of pions is the central source. The ratios $R_{\mathrm{I},\pi}$ show an only weak dependence on the PLA multiplicity. The trend of this dependence is as expected: The fraction of pions emitted from the central source slightly increases with decreasing impact parameter. The weakness of this increase suggests that for the selected centrality criteria

Table 3. Parameters of the three-source fits to the pion rapidity spectra for different PLA multiplicity bins. The labels $IQMD + GEANT$ refer to the filtered $IQMD$ simulations, the label $IQMD$(0.1) displays the unfiltered $IQMD$ simulation but with the $p_t > 0.1$ GeV/c cut included, the label $IQMD$ displays the unfiltered $IQMD$ simulation without any cut. The results under the label $thermal$ show the widths of thermal rapidity distributions with temperatures $T_{\mathrm{l},\pi}$ and with the $p_t > 0.1$ GeV/c cut included. Notice that the values for the widths σ are presented in units of $Y^{(0)}$. The numbers in parenthesis give the systematic error in the last 2 digits. The statistical error is of the order (05) for $R_{\mathrm{l},\pi}$ and (02) for $\sigma_{0,\pi}$, $\sigma_{1,\pi}$

		R_{l,π^-}	σ_{0,π^-}	σ_{1,π^-}	R_{l,π^+}	σ_{0,π^+}	σ_{1,π^+}
PM1	exp.	1.04(11)	0.42(04)	0.46(06)	1.47(24)	0.48(05)	0.49(05)
	GEANT	0.52(05)	0.45(02)	0.52(01)	0.54(07)	0.46(03)	0.52(01)
PM2	exp.	1.51(14)	0.45(04)	0.46(05)	1.39(29)	0.47(04)	0.43(03)
	GEANT	0.76(03)	0.47(05)	0.47(05)	0.80(06)	0.49(05)	0.53(04)
PM3	exp.	1.61(22)	0.47(05)	0.40(02)	1.40(16)	0.45(04)	0.43(05)
	GEANT	1.12(12)	0.55(02)	0.53(01)	0.88(03)	0.45(04)	0.51(01)
PM4	exp.	2.11(39)	0.47(05)	0.39(03)	1.67(38)	0.45(05)	0.42(04)
	GEANT	1.32(16)	0.51(05)	0.47(03)	1.12(04)	0.49(02)	0.51(01)
PM5	exp.	2.26(53)	0.46(05)	0.39(04)	1.92(77)	0.44(07)	0.40(05)
	GEANT	1.69(13)	0.49(02)	0.47(01)	1.59(15)	0.53(01)	0.48(01)
PM5D1	exp.	2.11(83)	0.46(08)	0.41(06)	1.88(96)	0.44(09)	0.42(06)
	GEANT	2.12(44)	0.54(04)	0.47(01)	3.55(84)	0.78(01)	0.52(02)
minimum	exp.	1.68(21)	0.45(04)	0.40(03)	1.52(14)	0.45(03)	0.42 (03)
bias	IQMD+GEANT	1.00(08)	0.48(02)	0.48(01)	0.90(04)	0.46(02)	0.50 (01)
	IQMD(0.1)	1.12(05)	0.55(02)	0.50(01)	0.95(04)	0.50(01)	0.49 (01)
	IQMD	0.79(09)	0.57(02)	0.60(01)	0.81(08)	0.58(02)	0.61 (01)
	thermal		0.69			0.72	

($PM5$) and ($PM5D1$) either the spectators have not completely disappeared or that the mechanism responsible for the longitudinal elongation of the pion momentum space distributions is particularly effective for near-central collisions. In addition the fitted values of the intensity ratio indicate that on the average the π^- are effected differently than the π^+, where the different pion charge may offer one possible explanation.

4 Discussion and comparison with $IQMD$

It is certainly true that charged pions from Au on Au collisions at 1 AGeV are primarily emitted from the central participant region. But the experimental observations provide ample evidence that subsequent processes of absorption and reemission in the surrounding spectator matter, termed rescattering, occur under all conditions. The most prominent indicators for such processes are the increase of the pion kinetic energies and of the pion yields at backward (and forward) directions of the participant frame. The probability for rescattering processes will depend on the relative fraction of nucleons bound in the participant and spectator regions, which in turn depends on the impact parameter and the nuclear density profile.

The investigation of the charged pion multiplicities as functions of participant number A_{part} revealed that to ignore the existence of a smooth nuclear surface leads to inconsistencies in the interpretation of the experimental observations. In order to reproduce the particle multiplicity n_{PLA} shown in Fig. 8 by the geometrical overlap of two Au nuclei with sharp surfaces, a nuclear radius $r = 1.35 \cdot A^{1/3}$ fm is required, in contradiction to the measured total cross section of 5.5 ± 0.5 barn. On the other hand if the radius is chosen to be $r = 1.14 \cdot A^{1/3}$ fm in accordance with the total cross section, the pion multiplicities n_π displayed in Fig. 9, become very nonlinear with A_{part} . As implied by Fig. 8, in this case n_{π^-} and n_{π^+} first rise fast with A_{part} for small values of A_{part} and then become almost constant for large values of A_{part}.

The natural conclusion is that nuclear surface effects play a role in the dynamics of relativistic nucleus-nucleus collisions. This was also pointed out 10 years ago in the review article of Stock [7]. Since the nuclear surface is a region of reduced nuclear density it is not evident a priori, that this region will participate in the nuclear stopping process for very central collisions, and that it will contribute to the high-density fireball. The experimental finding that the polar angular distributions of pions remain anisotropic for central collisions and that the spectator contributions to the rapidity spectra never vanish speak against this hypothesis. However, without the knowledge of the rescattering topology which has to include shadow and focussing effects, it is then impossible to predict the exact phase space distributions of charged pions from a simple model. Nevertheless, a limited insight might be gained with the help from a simplistic picture which assumes the existence of three thermal sources at target, fireball and projectile rapidities. The temperatures of these sources may be taken from the data, i.e. T = 30 MeV for the target and projectile spectators, and T = 45 MeV for the participant, which were obtained from a fit to the low energy portion of the pion spectra in subsection 3.2.2. Analyzed in the cm frame the resulting pion yields and kinetic energy spectra show similarities with the data as functions of the cm angle Θ.

In general the pion angular distribution from this very simple model rises for forward and backward angles due to the contributions from spectator sources. The pion kinetic energy distributions become harder for forward and backward angles although the source temperatures are smaller in the spectator regions than in the participant region. This apparent increase of the average kinetic energy is caused by the source velocities in the participant frame. The exact

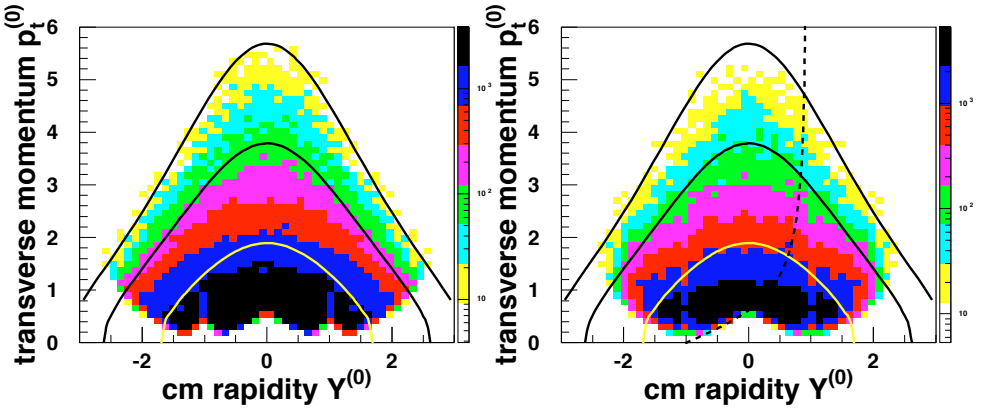

Fig. 20. The *left panel* shows the calculated distribution of charged pions in the $p_t^{(0)}$ versus $Y^{(0)}$ plane before the detector filter, the *right panel* shows the same distribution after having passed the detector filter. The definitions of the *shaded areas* and the curves are the same as in Fig. 10

form of these distributions depends very much on the relative yields of pions emitted from the spectator, respectively participant regions. If the pion yields from the sources at target respectively projectile rapidities are adjusted to $I_{1,\pi} = 1$, and from the central source to $I_{0,\pi} = 8$ then the resulting distributions resemble the measured data: The differential cross section $d\sigma/d\Omega$ increases at forward and backward angles $|\Theta - 90°| > 45°$ by roughly a factor 2, the energy distributions $1/PE \cdot d^2\sigma/dEd\Omega$ have concave shapes at these angles. On the other hand, at angles around 90° the distributions are close to thermal and spectator contributions can be neglected. These considerations are not meant to describe the dynamics of relativistic nucleus-nucleus collisions, and indeed, the resulting yield ratio $R_{\mathrm{I},\pi} = 4$ is outside the limits presented in Table 3, indicating that other phenomena like the forward-backward pion enhancement in the pp reaction [47] contribute. This anisotropy might survive in the low-density region of the nuclear surfaces where the number of nucleon - nucleon collisions becomes sufficiently small in near-central collisions. Nevertheless it is evident that part of the observations, including the increase of the apparent pion temperatures at backward angles, can be interpreted as due to rescattering phenomena in spectator matter.

A more thorough interpretation of the data requires the availability of a dynamical model capable of describing relativistic nucleus-nucleus collisions in full detail. For such a model we have chosen the $IQMD$ model [1, 9–12]. The $IQMD$ model is one of the existing models which describe the dynamic behaviour of heavy ion collisions at energies up to 1 AGeV. As already stated in Subsect. 2.3 this model was particularly developed to study pion production. But it was previously also employed by the $FOPI$ collaboration to study the production of light fragments (IMF) in central Au + Au collisions at energies between 150 and 800 AMeV [38]. From several choices this model with a hard equation of state (K = 380 MeV) and momentum dependent NN interaction gave the best agreement with the IMF experimental data. It is therefore reasonable that the same model with identical parameter values was used to test its predictive power on the pion results of the present experiment. The purpose of this test was therefore not to determine the best suited set of these parameters. But the outcome may point into the direction in which these parameters should be changed.

In the present comparison the values of the impact parameter b are chosen as to reproduce the 'minimum bias' condition. In general the results of the $IQMD$ calculation served as input for the $GEANT$ program with which the properties of the $FOPI$ detector are simulated. The comparison is therefore made between the measured results and the corresponding simulations which have passed the $GEANT$ filter. In this way differences between the experiment and the model cannot be attributed to the detector. On the other hand the properties of the detector and particularly the tracking procedures distort the original pion distributions to some extent. This may be seen in Fig. 20 which displays as contour plots of decreasing grey shades the calculated pion invariant cross sections $1/2\pi p_t \cdot d^2\sigma/dp_t dy$ in the left panel before they enter the $GEANT$ filter, and in the right panel after they have passed the $GEANT$ filter. In correspondence to Fig. 10 the cross sections are shown in a logarithmic scale, the full curves display the thermal distributions of pions with momenta 0.2, 0.4, 0.6 GeV/c, the dotted curve corresponds to the forward CDC boundary at $\vartheta = 30°$. Notice that the original $IQMD$ cross section is shown only within the symmetrized geometric boundaries of the CDC, it also includes the shadowing effects of the target. The CDC bias on the various quantities discussed in the previous subsections was studied in detail. In case of the extracted temperatures these bias corrections are of smaller size than the temperature variations with the emission angle and therefore remain within the stated errors. In case of the rapidity distributions the size of the corrections are listed in Table 3.

The largest impact parameter allowed in the Au + Au collisions determines the total cross section. In the present version of the $IQMD$ model this cross section is σ_{reac} = 5.34 barns in close agreement with the measured value $\sigma_{\mathrm{reac}} = 5.5 \pm 0.5$ barns. More indicative for the validity of the $IQMD$ model is the comparison of the reaction cross section as function of the particle multiplicity n_{PLA} measured with the forward detector PLA and shown in Fig. 6. Over the accepted multiplicity range the agreement between the measured and simulated data is quite satisfactory. Applying the same PM bins as in the experiment the $IQMD$ results were used to determine the average impact parameter for each bin. They are listed in Table 2 and may be compared to the corresponding results from the geometrical model. As had been established before [36, 37] the differences between these two estimates of the average impact parameters are

particularly large for the two most central multiplicity bins $PM5D1$ and $PM5$, the geometrical model underestimates the impact parameter here by over a factor 2. The conclusion from this discrepancy is that even the most central $PM5$ bin still includes reactions with impact parameters $b < 3$ fm. For the other multiplicity bins the geometrical model can be safely used to calculate the impact parameters.

The calculated pion multiplicities are shown as a function of A_{part} in Fig. 9. The procedure to obtain A_{part} from the simulated multiplicity n_{PLA} was the same as used with the experimental data and as demonstrated in Fig. 8. The error estimate was obtained by comparing the predictions of the geometrical and $IQMD$ models. It might be interesting to mention that the reproduction of the simulated cross section $\sigma(n_{\text{PLA}})$ by the geometrical model with surface parameter $a = 0$ requires a hard sphere radius $r_0 = 1.25$ fm, whereas the $IQMD$ initialization uses $r_0 = 1.12$ fm as was mentioned already in Subsect. 3.1. We have chosen the forward particle multiplicity n_{PLA} to obtain A_{part} since this multiplicity was used in previous works for the same purpose, particularly in the work of Harris et al. [50]. It was verified that by using $Z^{\text{bar}}_{\text{CDC}}$ the $IQMD$ predictions of the charged pion multiplicity remain within the uncertainty limits shown in Fig. 9. It is therefore evident that the pion multiplicities extracted from the $IQMD$ model with its present parameter values are too large when compared to the experiment. On the average the enhancement factor is $1.57 \pm 0.02 \pm 0.32$ both for π^- and π^+. This value and the quoted systematic error take into account the fact that the $IQMD$ model predicts a more linear relationship between the pion multiplicities and A_{part} than is found experimentally. Whereas this difference could be still caused by the uncertainties in deriving A_{part}, the overall reduction of the experimental pion multiplicities is believed to be outside the experimental errors. It should be remembered that the $IQMD$ results were passed through the complete detector filter. Furthermore the reduction is also observed in the other two experiments at GSI, $TAPS$ and $KaoS$ which have studied the same system at the same energy (see Fig. 9 and Fig. 11) [34, 46].

The fact that theoretical models tend to overpredict the pion multiplicities had been established before in lighter symmetric systems [7]. In the study of the $Ar + KCl$ and $La + La$ systems the pion multiplicities per A_{part} were found to scale simply with the cm bombarding energy per nucleon [50]. This universal energy law was used to extrapolate the previous pion results with lighter-mass systems into the Au + Au system at 1.06 AGeV. These so called Harris extrapolations are displayed in Fig. 9. They are in fair agreement with the corresponding $IQMD$ predictions and they therefore disagree with our experimental data for the Au + Au system. Since the size of the disagreement is similar for π^- and π^+ the corresponding ratios R_π from the data and the $IQMD$ model are in close agreement when the data are fitted by a linear function in A_{part}. However the experimental ratio R_π depends on A_{part}, it decreases with decreasing A_{part} as is clearly evident from Fig. 9. A comprehensive account of this dependence shall be presented in a forthcoming paper which also includes data from the ^{58}Ni + ^{58}Ni system. The ratio R_π is independent of A_{part} in the $IQMD$ model and it is constant by construction in the Harris extrapolation.

The observed dependence of R_E on the pion kinetic energies is very similar in the experiment and the model. Both are displayed in Fig. 13 where the data within the angular range $85° < \Theta < 135°$ were used to calculate R_E. For energies $E > 400$ MeV the statistical significance of the simulated results becomes too poor to allow a detailed comparison to the experimental data. The Fig. 13 nevertheless suggests that also the simulated R_E becomes constant at large energies, although probably at a somewhat higher value than the measured $R_E = 0.93 \pm 0.11$.

The measured and calculated transverse momentum spectra at midrapidity $|\Delta Y^{(0)}| < 0.2$ are displayed in Fig. 11. The $IQMD$ spectra have almost the identical shapes as the measured ones, however they are shifted to larger cross sections by a common factor of approximately 1.3. Considering the similar enhancement of the pion multiplicities this was to be expected. The reasons for the observed concave shapes were extensively studied with the help of the $IQMD$ calculations [11]. According to this model they are entirely due to the decay kinematics of the $\Delta(1232)$ resonance which is the only resonance included in the $IQMD$ model. Experimentally the dominance of the $\Delta(1232)$ resonance as pion source was recently confirmed at even higher AGS energies [51]. But the mass distribution of the **free** $\Delta(1232)$ resonance does not suffice to reproduce the transverse momentum spectra measured in the present experiment. In order to illustrate this point we have followed a procedure which was used by Schnedermann et al. [48] in the case of ultra relativistic heavy ion collisions. In this procedure the pions are assumed to originate in one part from resonance decays, where in the present case only the $\Delta(1232)$ is included, and in the other part from direct pions which are in thermal equilibrium with the hot participant matter. In the spirit of this model the freeze-out temperature is derived from the high-energy tail of the pion spectra, i.e. $T = 95$ MeV. The same temperature is assumed for the $\Delta(1232)$, collective flow effects on the resonance are therefore neglected. The omission of the collective velocity β_{col} might be allowed in this case since the kinetics of the pions is predominantly determined by the available decay energy from the $\Delta(1232)$ mass distribution. Furthermore the chosen value of the average kinetic energy of the $\Delta(1232)$ resonances is not too far off from the value one obtains with $T = 81 \pm 21$ MeV, $\beta_{\text{col}} = 0.32 \pm 0.05$ published for Au on Au collisions at 1 AGeV by the EOS collaboration [20]. The decomposition of the measured transverse momentum distribution of the π^- into pions from the $\Delta(1232)$ decay and into a possible contribution of direct pions is shown in Fig. 21. Pions emitted by the decay of the $\Delta(1232)$ resonance can almost completely account for the measured high-momentum tail of the spectrum Fig. 21, when the $\Delta(1232)$ mass distribution as parametrized by Ginocchio [53] is used. If direct pions are also emitted their contribution is estimated to be less than 5%, and it is more likely that the contribution from higher resonances than the $\Delta(1232)$ resonance is responsible for part of the pion yield beyond $p_t > 0.6$ GeV/c [30]. A more quantative analysis requires the freeze-out temperature to be better known. On the other hand the yield of soft pions can neither be explained by the decay of the $\Delta(1232)$ or higher resonances if those have the mass distributions of free resonances, nor can it be explained by direct pions. The observed

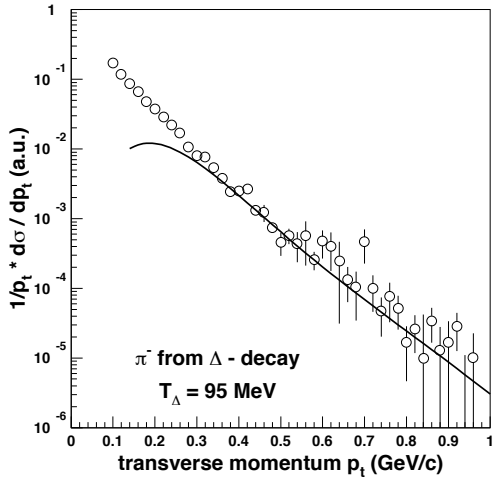

Fig. 21. Comparison of the measured π^- transverse momentum spectrum at midrapidity $|\Delta Y^{(0)}| < 0.1$ with the pion distribution from the decay of the free $\Delta(1232)$ resonance. The assumed fireball temperature is T = 95 MeV

enhanced yield of soft pions can only be explained in this scenario by a dramatic shift of the $\Delta(1232)$ mass to lower values, which was also pointed out by Senger [46].

It is obvious from Fig. 11 that the $IQMD$ model predicts the enhancement of the $\Delta(1232)$ strength at small masses. This is most likely not a true shift of the $\Delta(1232)$ mass distribution but caused by the time dependent change of the available phase space. In the early stages of the collision with its large dynamic compression, the $\Delta(1232)$ resonance is predominantly produced by protons of high energy and the pions emitted at this stage have large momenta. In later stages of the collision and after the fireball has cooled down the $\Delta(1232)$ resonance is predicted by the $IQMD$ model to be populated near the $N\pi$ threshold and the pions have therefore small momenta. Very recent results from the mass reconstruction of identified $\Delta(1232)$ resonances in the $p\pi$ channel seem to support this prediction [52]. These results indicate that pions with very small momentum are emitted from $\Delta(1232)$ resonances with masses close to the $N\pi$ threshold, whereas the decays of higher Baryon resonances are responsible for pions with large momenta. The origin of the soft-pion enhancement is a puzzle which has attracted considerable theoretical interest [54]. The explanation provided by the $IQMD$ model is a natural consequence of the cooling process during the expansion phase of the fireball, although other phenomena like the two-pion decay of resonances with masses larger than the $\Delta(1232)$ resonance might also contribute [55]. The effects of the dynamic evolution of the fireball should also be observable at higher energies. At AGS energies the discrepancy between the measured pion p_t distribution and its decomposition into contributions from direct pions and from pions of the $\Delta(1232)$ decay is only seen for transverse momenta $p_t < 0.05$ GeV/c, but in this analysis the pion spectra from the $\Delta(1232)$ decay were obtained with the help of $RQMD$ calculations and not from the mass distribution of the free $\Delta(1232)$ resonance [51].

It appears that the complex processes which govern the emission of pions from the fireball are fairly well described by the $IQMD$ model. This can be recognized in the angular distributions, where the observed forward and backward enhancement is reproduced by the $IQMD$ model, but not the weaker enhancement at midrapidity, see Fig. 16. The model traces the anisotropy of the angular distribution back to the presence of the projectile and target spectators. These are also responsible for the nonthermal shapes of the $1/2\pi p_t \cdot d^2\sigma/dp_t dy$ distributions, shown in Fig. 20. The corresponding experimental distributions, shown in Fig. 10, and their projections onto the rapidity axis, shown in Fig. 18, are the direct experimental illustration of the accepted scenario in which pions are emitted from three sources at $Y^{(0)} = 0$ and $Y^{(0)} = \pm 1$. The same hypothesis was used to fit the theoretical projections which are also displayed in Fig. 18. It is evident that their forms are in agreement with the three-source hypothesis. But their deviation from the thermal distribution with two pion temperatures is of a different type than found in the experiment, as demonstrated by the dotted curves in Fig. 18. The differences between the $IQMD$ calculations and the experiment have their origin in the relative strengths of the pion sources which are listed in Table 3. The widths of the rapidity distributions assigned to each of the three sources agree reasonably well between experiment and theory. It is the intensity ratio $R_{\mathrm{l},\pi}$ where one observes the largest difference, see Fig. 19: The experimental ratio $R_{\mathrm{l},\pi}$ is, except for central collisions, always larger than obtained from the $IQMD$ model. This implies that the rescattering phenomenon is experimentally not as strong as predicted by $IQMD$.

It should be noted that these conclusions are not an artefact of the detector filter. This may be seen from Table 3 where the $IQMD$ results are also listed without the $GEANT$ filter in two modes: $IQMD1$ includes the lower p_t threshold at $p_t > 0.1$ GeV/c which was applied to all the rapidity spectra, $IQMD2$ gives the unbiased results of the $IQMD$ model. The effect of the detector filter is to slightly reduce the participant contribution to the pion yields, whereas the p_t cut, as expected, causes the contributions from the spectators to be more excluded from the rapidity distributions than those from the participant. Therefore the contributions from the spectators are underestimated in the present analysis of the experimental data and of the filtered $GEANT$ results. These data definitively support the conclusion from the $IQMD$ calculation that the spectators have a nonnegligible influence on the emission pattern of pions. Notice that the widths of the fitted rapidity distributions, even after considering all possible corrections, are still smaller than expected for a thermal distribution with temperature $T_{\mathrm{l},\pi}$.

5 Summary and conclusions

In this paper the pion production in Au + Au collisions was studied at a bombarding energy of 1.06 AGeV. The pions were measured with the central drift chamber of the $FOPI$ detector at GSI, the disadvantage of not having the complete 4π coverage yet was bypassed by using the internal symmetry of the Au + Au system. The experimental data were compared to the corresponding predictions of the $IQMD$ model [1, 9–12]. This model was used in previous investigations by the $FOPI$ collaboration in which the production of intermediate mass fragments was studied in the identical

system but at lower energies [37, 38]. Since the employment of a drift chamber in heavy ion reactions requires complex tracking algorithms for particle identification, the tracking effects on the results were considered with the help of a detector filter which simulates the complete detection process in the $FOPI$ detector. All $IQMD$ predictions were passed through this filter.

The most striking disagreement between the experimental and $IQMD$ results was found for the pion multiplicities n_π. In both, experiment and theory, the pion multiplicities are observed to increase with the number of participants $A_{\rm part}$. This increase is almost linear in the $IQMD$ model and yields a π^- to π^+ ratio R_π = 1.95 in agreement with the prediction from isospin conservation $R_\pi = (N^2 + 5NZ)/(Z^2 + 5NZ)$. On the other hand , experimentally the ratios $n_\pi/A_{\rm part}$ are not constant but depend on $A_{\rm part}$, this dependence is different for π^- and π^+, and the average values of these ratios are smaller than the $IQMD$ predictions. Compared to the $IQMD$ predictions the reduction factor of $< n_\pi > / < A_{\rm part} >$ is 0.58 for π^-, and 0.67 for π^+. This implies that the measured average π^- to π^+ ratio is R_π = 1.69, i.e. smaller than predicted. This is due to the observed nonlinearity with $A_{\rm part}$. If the measured n_π values are fitted by a linear function in $A_{\rm part}$ then the experimental π^- to π^+ ratio agrees with the $IQMD$ prediction. Notice that the experimental π^- to π^+ ratio cannot be made independent of $A_{\rm part}$ when $A_{\rm part}$ is measured or determined by different methods.

Besides its $A_{\rm part}$ dependence the π^- to π^+ ratio was measured to depend also on the pion kinetic energies. It decreases first with growing energy to become constant with a value close to 1 at kinetic energies above 300 MeV. This dependence is also found with the $IQMD$ model, although there are differences between experiment and theory in the exact dependence on kinetic energy.

The positive pion multiplicities n_{π^+} determined in the present experiment agree with the results of the $KaoS$ collaboration which studied the identical system [46]. Assuming the correctness of the isobaryonic model they are also in accord with the neutral pion multiplicities measured by the $TAPS$ collaboration [34]. Since the results of $KaoS$ and $TAPS$ require the extrapolation from the midrapidity region into 4π there existed considerable doubt into the validity of the extracted multiplicity values since they depend on the validity of the thermal model used for the extrapolation. These values when compared to the results of the present experiment which measured charged pions in almost 4π are too small by roughly 13%. This relatively weak discrepancy, although the pion phase space distributions are non-thermal, is due to the complex behaviour of the pion angular distributions $\frac{d\sigma}{d\Omega}$. Under all conditions studied these distributions are strongly enhanced for forward and backward angles of the cm frame. This enhancement is also seen in the $IQMD$ calculations under 'minimum bias' condition. Experimentally one also observes a second, smaller enhancement at 90° in the cm system for pions of large kinetic energy, or for pions from central collisions. This second enhancement is not reproduced by the $IQMD$ model.

About the possible reasons why the pion multiplicities from the $IQMD$ model are larger than experimentally found, can at present only be speculated. Decisive for the pion yield is the thermal energy of the system. This energy was determined in a previous $FOPI$ publication [19, 37] to account for only 30% to 50% of the kinetic energies of fragments from the Au + Au reaction at energies lower than 1 AGeV, the rest of the energy is stored in collective flow. Similar results for the same system were obtained by the EOS collaboration [20]. A more conclusive explanation may be obtained once the fragment spectra of the present experiment are analyzed in detail. Another mechanism that might reduce the pion multiplicity is the strong pion absorption in nuclear matter. Strong pion absorption is the reason for the existence of several pion generations before the pion freeze out occurs. Pions are therefore a convenient probe to explore the nuclear matter distribution. For example the forward and backward enhancement of charged pions is, according to the $IQMD$ model, due to the remnants of target and projectile. These must then still exist in central collisions, probably because of the reduced density in the nuclear surface.

It is therefore not surprising that the distributions of pions in phase space were found to depend only weakly on the pion multiplicity. The pion results are therefore presented almost exclusively under 'minimum bias' condition. The $IQMD$ model reproduces these results in general, deviations are observed only in details. The main conclusions with respect to the pion production processes are then: Pions are dominantly produced by the decay of the $\Delta(1232)$ resonance, and pions from the fireball are partly absorbed and reemitted from the cold spectators. The first process is responsible for the concave shape of the pion kinetic energy spectra at angles close to 90° in the fireball frame. The shape is usually described by fitting two temperatures, a low temperature $T_{\rm l,\pi}$ and a high temperature $T_{\rm h,\pi}$, to the spectra. From the present experiment one obtains $T_{\rm l,\pi^-}$ = 42.2 MeV, $T_{\rm l,\pi^+}$ = 49.4 MeV and $T_{\rm h,\pi^-} = T_{\rm h,\pi_+}$ = 94.6 MeV. Following the $IQMD$ model pions with large energies are emitted early in the reaction from the $\Delta(1232)$ resonances populated at high masses, whereas pions with small energies are emitted later from the $\Delta(1232)$ resonances populated near the $N\pi$ threshold. The concave shape of the energy spectra is observed in many different systems, also in the $^{58}Ni+^{58}Ni$ system at various energies which will be discussed in a later publication. The strength of the high-temperature component seems to increase with system mass and bombarding energy which would indicate the growing importance of higher Baryon resonances. Whether or not this picture is correct needs further experimental confirmation besides the spectral shapes. Most directly it should be found in a sizeable shift in the invariant mass spectra of p, π pairs reconstructed for pions of low and high kinetic energies. First results from studies with the $FOPI$ detector which corroborate these conclusions were published in [52].

The shapes of the rapidity spectra $d\sigma/dy$ are nonthermal in the experiment as well as in the $IQMD$ calculation. They confirm the earlier suggestion that pions are emitted from secondary sources at smaller and larger rapidities than Y = 0. In the simplest scenario three pion sources were assumed at the rapidities of the central participant and the target-, respectively projectile spectators. Based on this assumption the fit of the measured rapidity distributions leads to the conclusion that the ratio between pions from the participant source to pions from the spectator sources slightly

decrease with impact parameter. This decrease is in agreement with $IQMD$ predictions, however the size of the ratio is larger in the experiment than in the $IQMD$ model. Rescattering phenomena in the spectator matter appear to be too strong in the model. On the other hand, the thermal assumption made to deduce this ratio is not well justified. For example, the widths of the fitted rapidity distributions when interpreted as temperature, yield values which are smaller than $T_{l,\pi}$. It is therefore rather questionable whether the picture of three sources in thermal equilibrium has any justification. Alternatively one could think of the colliding nuclei as an elongated system of nuclear matter with regions of different local temperatures and expansion velocities. Because of their short mean free path, the emission pattern of pions would strongly depend on the dynamic changes of the nuclear matter distribution and on the properties of the $\Delta(1232)$ and higher Baryon resonances. Such an approach, of course, does not provide an easy way to parametrize the experimental observations. The analysis of this $FOPI$ experiment is not yet complete and more may be learned about the appropriate approach from the ongoing analyses. They include the study of flow phenomena in the pion distributions, and correlation studies in the $\pi\pi$ and $p\pi$ pair channels. The latter should provide the needed information on the geometry of the pion sources and on the properties of the Δ resonances when they decay by pion emission.

This work was supported in part by the Bundesministerium für Forschung und Technologie under contract 06 HD 525 I(3) and by the Gesellschaft für Schwerionenforschung under contract HD Pel K. Additional support for the collaboration was providied by the Bundesministerium für Forschung und Technologie under project nos. X051.25, X081.25, and by the European Community under project no. ERBCIPD-CT40091.

References

1. S.A. Bass, C. Hartnack, H. Stöcker, W. Greiner, Phys. Rev. C **51**, 3343 (1995)
2. R.K. Puri, N. Ohtsuka, E. Lehmann, A. Fässler, H.M. Martin, D.T. Khoa, G. Batko, S.W. Huang, Nucl. Phys. **A536**, 201 (1992)
3. T. Maruyama, W. Cassing, U. Mosel, S. Teis, K. Weber, Nucl. Phys. **A573**, 653 (1994)
4. S. Nagamiya, M.-C. Lemaire, E. Moeller, S. Schnetzer, G. Shapiro, H. Steiner, I. Tanihata, Phys. Rev. C **24**, 971 (1981)
5. H.Stroebele, R. Brockmann, J.W. Harris, F. Riess, A. Sandoval, H.G. Pugh, L.S. Schroeder, R.E. Renfordt, K. Tittel, M. Maier, Phys. Rev. C **27**, 1349 (1983)
6. A. Baden, H.H. Gutbrod, H. Löhner, M.R. Maier, A.M. Poskanzer, T. Renner, H. Riedesel, H.G. Ritter, H. Spieler, A. Warwick, F. Welk, H. Wieman, Nucl. Instr. Meth. **203**, 189 (1992)
7. R. Stock, Phys. Rep. **135**, 259 (1986)
8. Bao-An Li, Nucl. Phys. **A552**, 605 (1993)
9. S.A. Bass, C. Hartnack, H. Stöcker, W. Greiner, Phys. Rev. C **50**, 2167 (1994)
10. C. Hartnack, L. Zhuxia, L. Neise, G. Peilert, A. Rosenhauer, H. Sorge, J. Aichelin, H. Stöcker, W. Greiner, Nucl. Phys. **A495**, 303 (1989)
11. J. Aichelin, Phys.Rep. **202**, 233 (1991)
12. J. Aichelin, G. Peilert, A. Bohnet, A. Rosenhauer, H. Stoecker, W. Greiner, Phys. Rev. C **37**, 2451 (1988)
13. J. Jaenicke, J. Aichelin, N. Ohtsuka, R. Linden, A. Fässler, Nucl. Phys. **A536**, 201 (1993)
14. B. Blättel, V. Koch, U. Mosel, Rep. Prog. Phys. **56**, 1 (1993)
15. W. Cassing, V. Metag, U. Mosel, K. Niita, Phys. Rep. **188**, 363 (1990)
16. V.N. Russkikh, Y.B. Ivanov, Y.E. Pokrovsky, P.A. Henning, Nucl. Phys. **A572**, 749 (1994)
17. P. Danielewicz, Phys. Rev. C **51**, 716 (1995)
18. W. Bauer, J.P.Bondorf, R. Donangelo, R. Elmer, B. Jakobssen, H. Schulz, F. Schussler, K. Snepper, Phys. Rev. C **47**, R1383 (1993)
19. FOPI collaboration: S.C. Jeong et al. Phys. Rev. Lett. **72**, 3468 (1994)
20. EOS collaboration: M.A. Lisa et al., Phys. Rev. Lett. **75**, 2662 (1995)
21. H.Stoecker, J. Phys. G. Nucl.Phys. **10**, L111 (1984)
22. H.Stoecker, W. Greiner, W. Scheid, Z. Physik A **286**, 121 (1978)
23. **TAPS** collaboration: R. Novotny et al., IEEE Trans. Nucl. Sci. **38**, 379 (1991)
24. KaoS collaboration: P. Senger et al., Nucl. Instr. Meth. **A327**, 393 (1993)
25. FOPI collaboration: J.P. Alard et al., Nucl. Instr. Meth. **A324**, 156 (1993)
26. KaoS collaboration: W. Ahner et al., Z. Phys. A **341**, 123 (1991)
27. KaoS collaboration: D. Brill et al., Phys. Rev. Lett. **71**, 336 (1993)
28. KaoS collaboration: D. Miskowicz et al., Phys. Rev. Lett. **72**, 3650 (1993)
29. KaoS collaboration: C. Müntz et al., GSI report GSI-93-41 (1993), and Z. Phys. A **352**, 175 (1995)
30. KaoS collaboration: C. Müntz et al., GSI Nachrichten GSI 10-95 (1995), page 11
31. TAPS collaboration: L.B. Venema et al., Phys. Rev. Lett. **71**, 835 (1993)
32. TAPS collaboration: O. Schwalb et al., GSI report GSI-93-38 (1993), and Phys. Lett. **B321**, 20 (1994)
33. TAPS collaboration: F.D. Berg et al., Phys. Rev. Lett. **72**, 977 (1994)
34. TAPS collaboration: V. Metag, private communication
35. DIOGENE collaboration: J.P. Alard et al., Nucl. Instr. Meth. **A261**, 379 (1987)
36. FOPI collaboration: J.P. Alard et al., Phys. Rev. Lett. **69**, 889 (1992)
37. FOPI collaboration: W. Reisdorf et al. to be published
38. FOPI collaboration: T. Wienold et al., GSI report GSI-94-74 (1994); also in: Hot and Dense Nuclear Matter, ed. W. Greiner, H. Stöcker and A. Gallmann (Plenum Press, 1994), page 289
39. FOPI collaboration: A. Poggi et al., Nucl. Phys. **A586**, 755 (1995)
40. FOPI collaboration: V. Ramillien et al., Nucl. Phys. **A587**, 802 (1995)
41. FOPI collaboration: J.L. Ritman et al., Z. Phys. A **352**, 355 (1995)
42. OPAL collaboration: K. Ahmet et al., Nucl. Instr. Meth. **A305**, 275 (1991)
43. GEANT3.15, $CERN$ Program Library Long Writeup W5013, CERN (1993)
44. K.G.R. Doss, H.A. Gustafsson, H.H. Gutbrod, K.H. Kampert, B. Kolb, H. Löhner, B. Ludewigt, A.M. Poskanzer, H.G. Ritter, H.R. Schmidt, H. Wieman, Phys. Rev. Lett. **57**, 302 (1986)
45. R. Hofstatter, Rev. Mod. Phys. **28**, 214 (1956)
46. P. Senger, in: Multiparticle Correlations and Nuclear Reactions, ed. by J. Aichelin and D. Ardouin (World Scientific Publ. Co., 1994), page 285
47. K.L. Wolf, H.H. Gutbrod, W.G. Meyer, A.M. Poskanzer, A. Sandoval, R. Stock, J. Gosset, C.H. King, G. King, Nguyen Van Sen, G.D. Westfall, Phys. Rev. Lett. **42**, 1448 (1979)
48. E. Schnedermann, J. Sollfrank, U. Heinz, Phys. Rev. C **48**, 2462 (1993)
49. Bao-An Li, Phys. Lett. B **319**, 412 (1993)
50. J.W. Harris, G. Odyniec, H.G. Pugh, L.S. Schroeder, M.L. Tincknell, W. Rauch, R. Stock, R. Bock, R. Brockmann, A. Sandoval, H. Ströbele, R.E. Renfordt, D. Schall, D. Bangert, J.P. Sullivan, K.L. Wolf, A. Dacal, C. Guerra, M.E. Ortiz, Phys. Rev. Lett **58**, 463 (1987)
51. E814 collaboration: J. Barrette et al., Phys. Lett. B **351**, 93 (1995)
52. FOPI collaboration: M. Eskef et al., GSI report GSI-96-1 (1996), page 44
53. J.N. Ginocchio, Phys. Rev. C **17**, 195 (1978)
54. V. Koch, G.F. Bertsch, Nucl. Phys. **A552**, 591 (1993)
55. S. Teis, W. Cassing, M. Effenberger, A. Hombach, U. Mosel, G. Wolf, GSI report GSI-95-1 (1995), page 89

This article was processed by the author using the LaTeX style file *pljour2* from Springer-Verlag.